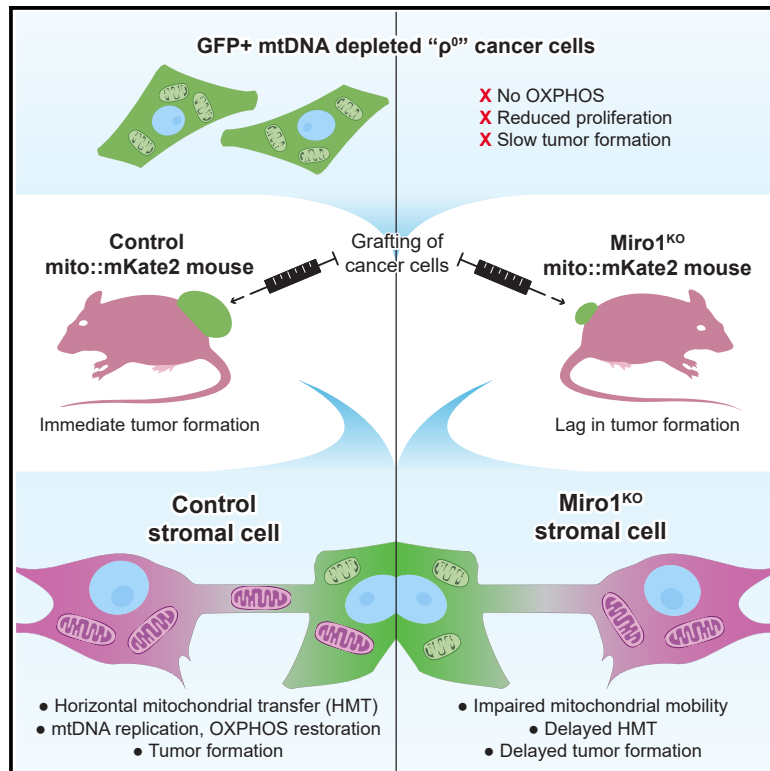


The adaptor protein Miro1 modulates horizontal transfer of mitochondria in mouse melanoma models

Graphical abstract



Authors

Jaromir Novak, Zuzana Nahacka, Gabriela L. Oliveira, ..., Stepana Boukalova, Jakub Rohlena, Jiri Neuzil

Correspondence

zuzana.nahacka@ibt.cas.cz (Z.N.), j.neuzil@griffith.edu.au (J.N.)

In brief

Novak et al. show how Miro1 regulates mitochondrial transfer from the tumor microenvironment to mtDNA-deficient melanoma cells. The authors argue that delayed tumor formation observed in Miro1^{KO} mice results from impaired mitochondrial transfer, which involves reduced microtubule association, disruption of the mitochondrial network, and TNT formation.

Highlights

- Miro1 regulates HMT and tumor growth in melanoma cells
- Miro1^{KO} reduces mitochondrial association with microtubules
- Miro1^{KO} disrupts mitochondrial mobility and positioning
- TNTs facilitate HMT in melanoma cancer



Article

The adaptor protein Miro1 modulates horizontal transfer of mitochondria in mouse melanoma models

Jaromir Novak,^{1,2,17} Zuzana Nahacka,^{1,17,*} Gabriela L. Oliveira,^{1,3,4,5} Petra Brisudova,^{1,2} Maria Dubisova,^{1,2} Sarka Dvorakova,¹ Sona Miklovicova,^{1,2} Marketa Dalecka,² Verena Puttrich,¹ Lenka Grycova,¹ Silvia Magalhaes-Novais,^{1,6} Catarina Mendes Correia,⁷ Jennifer Levoux,⁸ Ludek Stepanek,⁶ Jan Prochazka,⁶ David Svec,¹ David Pajuelo Reguera,⁶ Guillermo Lopez-Domenech,⁹ Renata Zobalova,¹ Radek Sedlacek,⁶ Mikkel G. Terp,¹⁰ Payam A. Gammage,^{7,11} Zdenek Lansky,¹ Josef Kittler,⁹ Paulo J. Oliveira,^{3,4} Henrik J. Ditzel,^{10,12} Michael V. Berridge,¹³ Anne-Marie Rodriguez,^{8,14} Stepana Boukalova,^{1,2} Jakub Rohlena,¹ and Jiri Neuzil^{1,2,15,16,18,*}

¹Institute of Biotechnology, Czech Academy of Sciences, 252 50 Prague-West, Czech Republic

²Faculty of Science, Charles University, 128 00 Prague, Czech Republic

³NC-UC, Center for Neuroscience and Cell Biology, University of Coimbra, 3060-197 Cantanhede, Portugal

⁴CIBB, Centre for Innovative Biomedicine and Biotechnology, University of Coimbra, 3060-197 Cantanhede, Portugal

⁵Institute for Interdisciplinary Research, Doctoral Program in Experimental Biology and Biomedicine (PDBEB), University of Coimbra, 3060-197 Cantanhede, Portugal

⁶Czech Center for Phenogenomic, Institute of Molecular Genetics, Czech Academy of Sciences, 252 50 Vestec, Czech Republic

⁷Cancer Research UK Scotland Institute, Glasgow G61 1BD, UK

⁸Sorbonne University, Institute of Biology Paris-Seine, 75005 Paris, France

⁹Department of Neuroscience, Physiology and Pharmacology, University College London, Gower Street, London WC1E 6BT, UK

¹⁰Institute of Molecular Medicine, University of Southern Denmark, 5000 Odense, Denmark

¹¹School of Cancer Sciences, University of Glasgow, Glasgow G61 1BD, UK

¹²Department of Oncology, Odense University Hospital, 5000 Odense, Denmark

¹³Malaghan Institute of Medical Research, Wellington 6012, New Zealand

¹⁴University Paris-Est Créteil, INSERM, IMRB, 94010 Créteil, France

¹⁵School of Pharmacy and Medical Science, Griffith University, Southport, QLD 4222, Australia

¹⁶1st Faculty of Medicine, Charles University, 121 08 Prague, Czech Republic

¹⁷These authors contributed equally

¹⁸Lead contact

*Correspondence: zuzana.nahacka@ibt.cas.cz (Z.N.), j.neuzil@griffith.edu.au (J.N.)

<https://doi.org/10.1016/j.celrep.2024.115154>

SUMMARY

Recent research has shown that mtDNA-deficient cancer cells (ρ^0 cells) acquire mitochondria from tumor stromal cells to restore respiration, facilitating tumor formation. We investigated the role of Miro1, an adaptor protein involved in movement of mitochondria along microtubules, in this phenomenon. Inducible Miro1 knockout (Miro1^{KO}) mice markedly delayed tumor formation after grafting ρ^0 cancer cells. Miro1^{KO} mice with fluorescently labeled mitochondria revealed that this delay was due to hindered mitochondrial transfer from the tumor stromal cells to grafted B16 ρ^0 cells, which impeded recovery of mitochondrial respiration and tumor growth. Miro1^{KO} led to the perinuclear accumulation of mitochondria and impaired mobility of the mitochondrial network. *In vitro* experiments revealed decreased association of mitochondria with microtubules, compromising mitochondrial transfer via tunneling nanotubes (TNTs) in mesenchymal stromal cells. Here we show the role of Miro1 in horizontal mitochondrial transfer in mouse melanoma models *in vivo* and its involvement with TNTs.

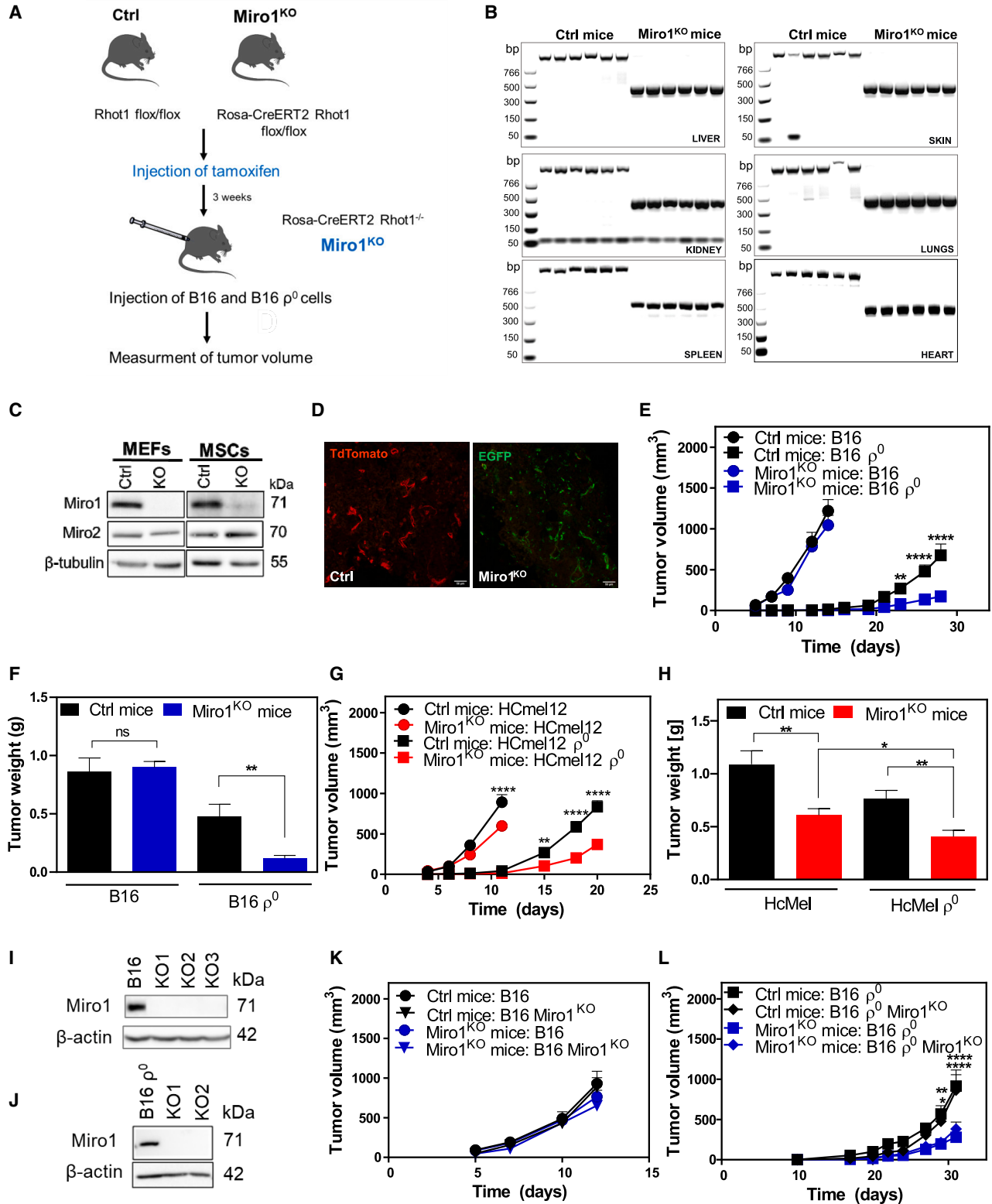
INTRODUCTION

Cancer is the second most frequent cause of death with rising incidence and mortality worldwide.^{1,2} Early observations of tumor cells exhibiting glycolytic metabolism have now been superseded by more dynamic real-time metabolic remodeling influenced by the tumor microenvironment.^{3–6} In addition to glucose, other substrates including amino acids such as glutamine and fatty acids are widely used to fuel tumor growth and

progression.^{7–10} Cancer cells require the tricarboxylic acid cycle and oxidative phosphorylation (OXPHOS), both of which are compartmentalized in mitochondria for intermediates of various metabolic pathways and for their bioenergetic needs.^{11–15} Mitochondrial targeting is therefore considered a promising strategy for cancer therapeutic development.¹⁶

Recent research has revealed a phenomenon referred to as horizontal mitochondrial transfer (HMT), where cells with dysfunctional mitochondria acquire functional mitochondria





(legend on next page)

from neighboring cells.^{17–20} This field was stimulated by a landmark publication demonstrating movement of organelles between cells.^{21,22} Functionally, HMT was first reported in a co-culture of human bone marrow-derived non-hematopoietic stromal cells (MSCs) or skin fibroblasts and lung cancer cells devoid of mitochondrial DNA (ρ^0 cells), resulting in recovery of respiration in the cancer cells.²³ This was followed by other *in vitro* demonstrations of HMT and its link to mitochondrial function.^{17,24–28} Notably, MSCs have been identified as mitochondrial donors in most studies investigating HMT, including our *in vitro* findings.^{17,29–31} Furthermore, we have unequivocally shown HMT in mouse tumor models, in which ρ^0 cells import functional mitochondria with their mtDNA payload from donor cells to restore respiration. This was shown to be associated with recovery of *de novo* pyrimidine biosynthesis.^{29,32,33} HMT has also been demonstrated in the context of cancer therapy.^{25,34} Mechanistically, cells can acquire mitochondria in multiple ways, e.g., via cell fusion, vesicular transfer, gap junctions, and most frequently, via tunneling nanotubes (TNTs), which are intercellular bridges connecting the cytoplasm of two cells.^{17,35,36}

Mitochondrial movement has been extensively studied in neuronal cells, where it has been shown that mitochondria move within cells along actin filaments and microtubules, the latter being crucial for traversing long distances.^{37–39} The adaptor protein Miro1 (encoded by the *RHOT1* gene), together with its counterpart Miro2 (encoded by *RHOT2* gene), is a crucial adaptor protein transporting mitochondria in cells.^{39,40} Both proteins are part of a Rho GTPase family, localized in the outer mitochondrial membrane.⁴¹ They possess two GTPase domains and two EF-hand motifs that bind calcium, thereby facilitating the release of mitochondria from the cytoskeleton and their immobilization in response to high calcium levels.^{42–44} Along these, Miro1 and Miro2 are important regulators of calcium homeostasis, communication with the endoplasmic reticulum, and PINK1/Parkin-mediated mitophagy.^{39,40} Research indicates that cells primarily rely on Miro1 for the long-distance transport of mitochondria along microtubules,³⁸ while Miro2 plays a less significant role in this process, making Miro1 the focal point of this study.

The role of Miro1 and its involvement in cancer and particularly HMT is less well understood. Several studies have reported up-regulation of Miro1,^{45–52} and to a lesser extent Miro2,⁵³ in various

cancers, linking their increased expression on the RNA or protein level to enhanced cell proliferation, invasiveness, and metastasis, suggesting that Miro1 supports the aggressive behavior of tumor cells by modulating either distinct signaling pathways via circRNA or on a protein level via mitochondrial dynamics and cellular energy distribution.⁵⁴

In this study, we present the comprehensive investigation of the role of Miro1 in the rescue of melanoma cancer cells without mtDNA via the process of HMT *in vivo*. Using a Miro1 knockout (KO) model, we demonstrate the impact of Miro1, absent in the tumor stroma, on tumor growth and frequency of mitochondrial transfer, which is further supported by using a cell-free, reconstituted system. Finally, our findings elucidate a molecular mechanism involved in cancer progression, opening an avenue for potential therapeutic interventions.

RESULTS

Miro1 depletion in tumor stroma delays tumor formation by B16 ρ^0 and HCmel12 ρ^0 cells

To investigate the potential involvement of Miro1 in mitochondrial dynamics and HMT regulation in cancer, we generated an inducible whole-body Miro1 KO (Rhot1 Rosa-CreERT2 or Miro1^{KO}) mouse strain on the background of the C57BL/6 mouse (see STAR Methods; Figure 1A). This model offers a valuable opportunity to study the effects of Miro1^{KO} specifically in donor cells, which provide mitochondria to cancer cells via HMT. Given that Miro1^{KO} has been reported to be embryonically lethal,^{38,55} we used tamoxifen-inducible *RHOT1* gene KO mediated by the ROSA26/*Cre-loxP* recombination^{56–59} (see STAR Methods). We verified *RHOT1* gene (coding for the Miro1 protein) deletion in various organs at both the DNA (Figures 1B and S1A) and protein level (Figure S1B), demonstrating Miro1 depletion in nearly all organs (Figures 1B and S1B), but not brain, where we observed little if any change of Miro1 (Figures S1A and S1B). Further, we observed deletion of Miro1 in our two cellular models, mouse embryonic fibroblasts (MEFs) and MSCs isolated from uninduced Rhot1 Rosa-CreERT2 mice following their treatment with hydroxytamoxifen *in vitro* (Figure 1C). As discussed in a previous article, MSCs have been shown to act as mitochondrial donors in *in vitro* studies,^{23,29} making them particularly relevant for our investigation. Further, we investigated whether Miro1^{KO} influences mitochondrial function both *in vitro*

Figure 1. Miro1 depletion in tumor stroma delays tumor formation by B16 ρ^0 and HCmel12 ρ^0 cells

(A) *RHOT1* (Miro1) deletion strategy and design of *in vivo* experiments.

(B) *RHOT1* DNA detection in different organs ($n = 6$).

(C) Western blot analysis of Miro1 levels in MEFs and MSCs ($n = 3$).

(D) Confocal fluorescence images of Miro1 depletion in B16 tumor stroma of reporter dTomato/EGFP mouse, Ctrl/ $n = 1$, Miro1^{KO}/ $n = 2$, four different cryosections per each mouse, scale bar, 50 μm .

(E and F) Tumor growth of B16 and B16 ρ^0 cells. (E) Ctrl and Miro1^{KO} mice were grafted with B16 and B16 ρ^0 (B16/ $n \geq 8$, B16 ρ^0 / $n = 15$) for each group. (F) Tumor weight, B16/ $n \geq 4$, B16 ρ^0 / $n = 10$) for each group.

(G and H) Tumor growth of HCmel12 and HCmel12 ρ^0 cells. (G) Ctrl and Miro1^{KO} mice were grafted with HCmel12 and HCmel12 ρ^0 cells (HCmel12/ $n \geq 16$, HCmel12 ρ^0 / $n = 16$) for each group. (H) Tumor weight, HCmel12/ $n \geq 16$, HCmel12 ρ^0 / $n = 16$) for each group.

(I and J) Western blot analysis of different (I) B16 Miro1^{KO} and (J) B16 ρ^0 Miro1^{KO} clones ($n = 3$).

(K) Tumor growth of B16 Miro1^{KO} cells. Ctrl and Miro1^{KO} mice were grafted with B16 and B16 Miro1^{KO} cells (three different clones) (B16/ $n = 12$, B16 Miro1^{KO}/ $n \geq 25$) for each group).

(L) Tumor growth of B16 ρ^0 Miro1^{KO} cells. Ctrl and Miro1^{KO} mice were grafted with B16 ρ^0 and B16 ρ^0 Miro1^{KO} cells (2 different clones) (B16 ρ^0 / $n = 13$, B16 ρ^0 Miro1^{KO}/ $n = 22$) for each group. Unpaired t test (F, H) or two-way ANOVA with Sidak's multiple comparisons test (E, G, K, L).

Data are presented as mean values \pm SEM. * $p < 0.05$, ** $p < 0.01$, *** $p < 0.001$, **** $p < 0.0001$. ns, not significant. See also Figure S1.

and *in vivo*. For these analyses, we used MEF cells, along with adult tissues that either had high mitochondrial content or were anatomically proximal to the site of subcutaneous melanoma cell injection used in subsequent experiments. Using MitoTracker staining, we detected an increase in mitochondrial content (Figure S1C) in MEF cells with Miro1^{KO}, accompanied by a small non-significant decrease in mitochondrial membrane potential (Figure S1D). However, mitochondrial respiration, including routine respiration, complex I, and complex II activity, remained unchanged (Figure S1E). Interestingly, adult tissues with Miro1^{KO} in cells showed no changes in mitochondrial content (Figure S1F), mitochondrial membrane potential (Figure S1G), or any aspect of mitochondrial respiration (Figure S1H).

We then explored the premise that Miro1 deletion within the tumor microenvironment, specifically in the tumor stroma serving as a potential source of mitochondria for transfer to cancer cells without mtDNA (ρ^0 cells), affects HMT. We used transgenic reporter mouse dTomato/EGFP with Miro1^{KO} (see STAR Methods), with expression patterns dependent on the KO status (dTomato indicating no recombination and EGFP indicating recombination). We then grafted B16 melanoma cells and collected tumor samples after 14 days. Using this experimental approach, we successfully detected positive dTomato expression but negative EGFP expression in cryosections of tumors isolated from control (Ctrl) mice, while observing the opposite in Miro1^{KO} animals (Figure 1D). This finding suggests specific and controlled deletion of Miro1 within the tumor microenvironment and stromal cells, facilitating the possibility of manipulating mitochondria donors in the tumor context.

Our earlier study introduced a model of severe mitochondrial genome damage leading to absence of mtDNA (B16 ρ^0 cells).³³ We demonstrated that subcutaneous grafting of B16 ρ^0 cells into syngeneic C57BL/6 mice resulted in the formation of tumors after a delay of 2–3 weeks compared with B16 cells, triggered by HMT in the tumor microenvironment and respiration recovery.^{17,32,33} To assess the role of Miro1 in the process of HMT, we injected both Ctrl and Miro1^{KO} mice with B16 and B16 ρ^0 cells and monitored tumor growth (Figure 1E). Notably, we not only confirmed the previously observed 2- to 3-week delay in tumor growth for B16 ρ^0 cells compared with the respiration-competent parental B16 cells, but also observed an additional delay in the onset of tumor formation in Miro1^{KO} mice with slower tumor growth when compared with Ctrl mice (Figure 1E). The slower kinetics of tumor formation was supported by significantly lower tumor mass measured at the endpoint of the experiment (Figure 1F).

We confirmed that the observed differences were not a consequence of increased cell death in the tumor stroma (Figure S1I), but possibly stemmed from variations in the proliferative capacity of tumor cells. Importantly, this phenomenon was not detected in the case of respiratory-competent B16 cells grafted into both Ctrl and Miro1^{KO} mice (Figures 1E and 1F).

In addition to B16 cells, we conducted tumor growth experiments using HcMel12 and HcMel12 ρ^0 cell line (Figures 1G, S1J, and S1K), another well-established melanoma model with distinct genetic characteristics. In these experiments, ρ^0 -derived tumors showed again significantly slower growth kinetics when injected into Miro1^{KO} mice compared withCtrls (Figures 1G

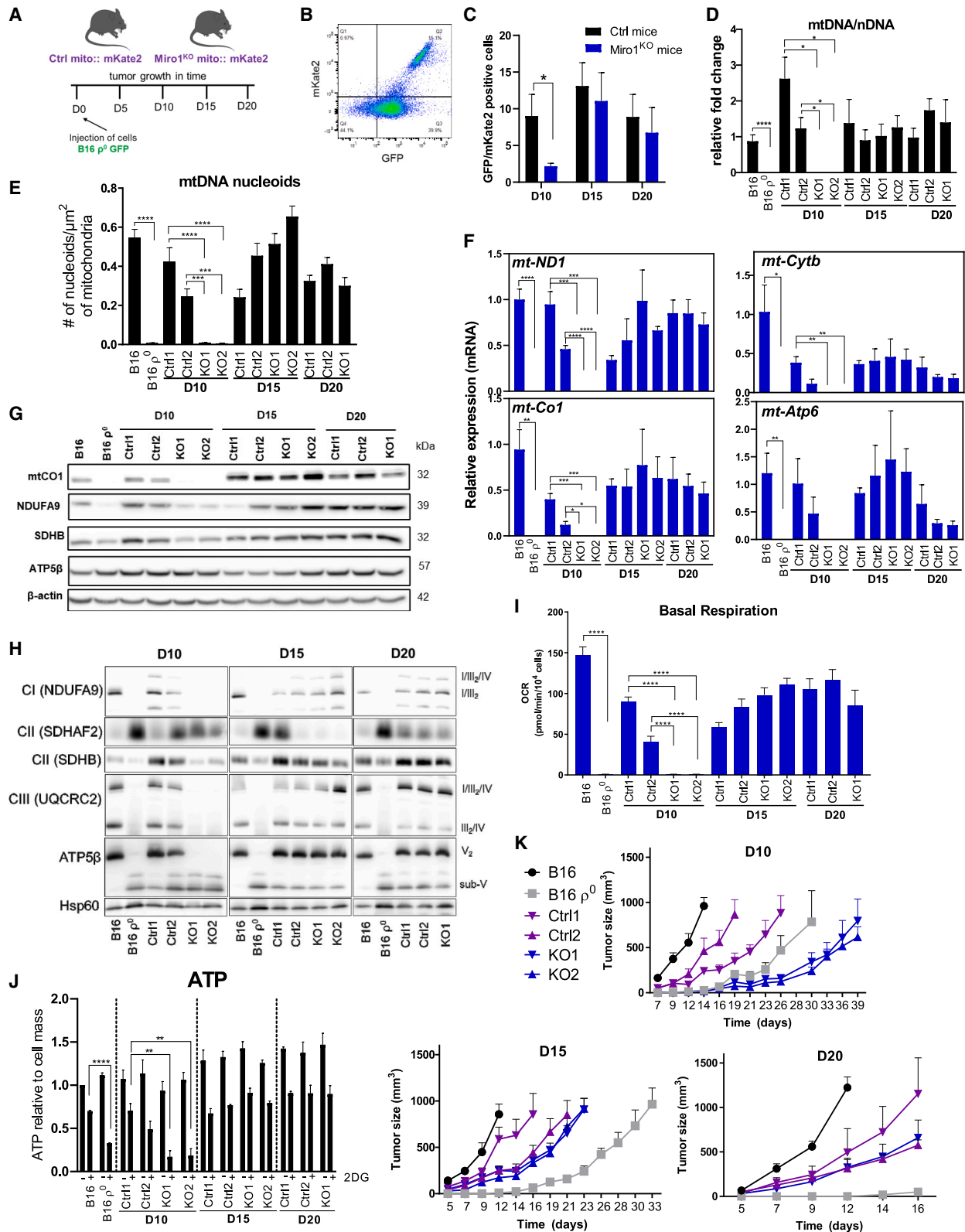
and 1H). These findings demonstrate the reproducibility of our results across two different melanoma models. Unlike in the B16 model, parental HcMel12 cells also showed reduced tumor growth in Miro1^{KO} mice, possibly due to decreased liver metabolism in KO mice affecting tumor proliferation in a cell type-specific manner (see STAR Methods). Importantly, we observed a significant difference in tumor weight between HcMel12 and HcMel12 ρ^0 isolated from KO mice (Figure 1H), indicating that Miro1 deletion differentially affects the growth of these two tumor types.

Next, we asked whether absence of Miro1 in recipient cancer cells could affect HMT. To accomplish this, we used CRISPR-Cas12 technology to generate B16 and B16 ρ^0 cells without Miro1 protein (Figures 1I and 1J, respectively). Previous publications have shown that Miro1 or Miro1/Miro2 depletion may affect cell division and bioenergetics (cristae structure) *in vitro*.^{38,55,60} We therefore assessed proliferation of Miro1-deficient B16 and B16 ρ^0 cells (Figure S1L). We identified differences in proliferation in one of the three clones of B16 Miro1^{KO} and in one of the two clones of B16 ρ^0 Miro1^{KO} cells (Figure S1L), possibly resulting from clonal variability of the cells. Additionally, we found no discernible differences for any of Miro1^{KO} clones compared with parental B16 cells in respiration or enzymatic activities of mitochondrial respiratory complexes, as well as cristae structure and morphology (Figures S1M and S1N). Finally, as in the previous experiments, we injected these modified cells into both Ctrl and Miro1^{KO} mice and assessed tumor progression (Figures 1K and 1L). In none of these cases did we find any additional significant effect of Miro1 deletion in recipient cells on tumor growth for either B16 (Figures 1K and S1O) and B16 ρ^0 cells (Figures 1L and S1P).

Our results are consistent with the hypothesis that slower kinetics of tumor formation observed in Miro1^{KO} mice injected with both B16 ρ^0 and HcMel12 ρ^0 cells, relative to Ctrl mice, could potentially be due to reduced mitochondrial transfer from tumor stroma, which we investigated in detail in subsequent experiments.

Miro1 depletion reduces the horizontal transfer of mitochondria to B16 ρ^0 cells during the initial stages of tumor development

To further address the impact of Miro1^{KO} on HMT, we generated transgenic mice bearing heterozygous expression of the mito::mKate2 far-red fluorescent protein targeted to mitochondria. For this purpose, we cross-bred both Ctrl and Rhot1 Rosa-CreERT2 mice with C57BL/6J mito::mKate2 mice⁶¹ (see STAR Methods). Notably, we found no negative effect of mito::mKate2 protein on mitochondrial function in various organs compared with Ctrl mice (Figures S2A and S2B). We know from our previous work^{17,32,33} that mitochondrial transfer occurs in the initial days after grafting ρ^0 cancer cells. In order to detect mitochondrial transfer from tumor stromal cells to cancer cells, we grafted B16 ρ^0 cells with cytoplasmic expression of GFP into Ctrl/mito::mKate2 and Miro1^{KO}/mito::mKate2 mice. We then harvested tumor plaques at early time points of tumor development, as depicted in Figure 2A, and evaluated them by fluorescent cytometry (Figures 2B, 2C, S2C, and S2D) and confocal microscopy (Figure S2E). Our analysis revealed the presence of GFP-positive cells that acquired mKate2-positive mitochondria



(legend on next page)

from tumor stromal cells (Figures 2B and S2E), referred to as double-positive cells. Notably, tumor plaques isolated on day 10 (D10) derived from Miro1^{KO} mice showed a significantly lower number of GFP/mKate2 double-positive cells than those isolated from Ctrl mice (Figure 2C). Non-significant differences in the number of double-positive cells were found in tumor tissues isolated on D15 and D20 after grafting from Ctrl and Miro1^{KO} mice (Figure 2C).

The previously mentioned results prompted us to assess the level of mtDNA in cell lines derived from these tumors. mtDNA, absent in B16 ρ^0 cells, was found to be considerably higher in cells derived from Ctrl mice compared with Miro1^{KO} mice on D10 after grafting (Figures 2D and 2E). Similarly, analysis of mitochondrial mRNA (Figure 2F) and protein expression of mtDNA- and nuclear DNA-encoded subunits of mitochondrial respiration complexes (Figures 2G and S2F) revealed a similar pattern. To establish a possible link between restoration of tumor-forming capability and the rates of respiration and glycolysis, all derived cell lines (D10–D20) were analyzed for the assembly of respiratory complexes (Figure 2H) and assessed by high-resolution respirometry (Figures 2I and S2G), as well as for generation of ATP via OXPHOS and glycolysis (Figure 2J). These data support previous results from Figure 2C and are consistent with mtDNA levels (cf. Figures 2D and 2E).

We next queried whether differences in HMT observed in tumor samples between Ctrl and Miro1^{KO} mice were reflected in the growth of cell lines isolated on D10, D15, and D20 (Figures 2K, S2H, and S2I). We grafted C57BL/6J mice with B16, B16 ρ^0 and D10, D15 and D20 cells (isolated from both Ctrl and Miro1^{KO} mice), and monitored tumor growth. Remarkably, Ctrl/D10 cells exhibited a faster growth rate than B16 ρ^0 but at a slower rate than B16 cells (Figure 2K). In contrast, Miro1^{KO}/D10 cells exhibited a significantly reduced growth rate, similar to B16 ρ^0 cells, in line with earlier findings that these cells have very low, or no mtDNA respectively (see above). Interestingly, both groups of cells derived on D15 (Figure 2K) formed tumors faster than B16 ρ^0 cells, while Ctrl/D15 cells exhibited greater tumor-forming potential when compared with cells derived from tumors grown in Miro1^{KO} mice. Analysis of proliferation rates of all tumor-derived cell lines, including B16 and B16 ρ^0 cells, was consistent with the tumor growth kinetics observed *in vivo* (Figures 2K, S2H, and S2I).

Taken together, we show that Miro1 modulates HMT at initial time points after grafting of tumor cells. Our findings reveal a significant reduction in mitochondria acquired by tumor cells without mtDNA following grafting into Miro1^{KO} mice, supported by differences in the level of mtDNA, expression of respiratory complexes, mitochondrial respiration, and proliferation of the cells derived from individual tumor plaques during initial stages of tumor formation. Miro1 therefore modulates the ability of cancer cells lacking mtDNA to acquire mitochondria from tumor stroma and to restore their tumor-forming capacity.

Miro1 impacts localization and dynamics of mitochondrial network

To explore the molecular mechanism responsible for the role of Miro1 in HMT, we used a reconstituted cell-free system (Figures 3A and S3A) as described previously.^{62,63} Briefly, microtubules, the molecular motor kinesin KIF5B and the adaptor protein TRAK1 were combined with mitochondria isolated from liver of Ctrl and Miro1^{KO} mice, B16 and B16 Miro1^{KO} cells, or B16 ρ^0 and B16 ρ^0 Miro1^{KO} cells. Subsequent analysis of mitochondrial movement revealed that absence of Miro1 led to significantly reduced number of mitochondria progressively moving along microtubules (referred to as the landing rate) using mouse liver and B16 cell-derived mitochondria (Figures 3B and 3C). However, we observed no significant differences in other parameters including velocity, run time, and run length when mitochondria were extracted from B16 cells and mouse liver tissue, and no difference in all parameters including landing rate for B16 ρ^0 cell mitochondria (Figure S3B).

To investigate the impact of Miro1 deficiency on spatial distribution of the mitochondrial network in various cell types, we implemented a method based on seeding cells onto Y-shaped micropatterned chips.⁶⁴ We conducted Sholl-based analysis of mitochondrial positioning with respect to the cell nucleus.³⁸ Absence of Miro1 resulted in aggregation of mitochondria in the perinuclear region, leading to their absence in the cellular periphery (Figures 3D, 3E, and S3C). This effect was observed in both MSCs and MEFs derived from Ctrl and Miro1^{KO} mice, as well as in B16 cells (Figure 3F), but not in B16 ρ^0 cells (Figure S3D). Notably, we observed the same effect in MSCs with Miro1 deletion, whether it was induced *in vitro* or *in vivo* (Figure 3F; see also STAR Methods).

Figure 2. Miro1 depletion reduces the horizontal transfer of mitochondria to B16 ρ^0 cells during the initial stages of tumor development

(A) Scheme of experimental setup. Ctrl and Miro1^{KO} mice, both mito::mKate2, were grafted with B16 ρ^0 GFP cells. Tumors were dissected at various time points as depicted.

(B and C) Fluorescent cytometry analysis for mKate2⁺/GFP⁺ (PE⁺/FITC⁺) double-stained population. (C) Quantification of the mKate2⁺/GFP⁺ population for individual tumor plaques harvested from Ctrl and Miro1^{KO} mice ($n \geq 5$ for each group).

(D) mtDNA detection by qPCR in individual cancer cell lines derived as depicted in (A) ($n \geq 3$). Presented data are relative to nDNA.

(E) mtDNA nucleoids in individual cancer cell lines derived as depicted in (A) taken by confocal microscopy, $n \geq 5$ fields of view per cell line for each experiment ($n = 2$). Presented data are normalized to area of the mitochondrial network.

(F and G) Expression of mtDNA and nDNA encoded OXPHOS subunits. (F) qRT-PCR ($n \geq 3$). (G) Western blot ($n = 3$).

(H) NBGE depicting the assembly of respiration complexes and supercomplexes in tumor-derived cell lines ($n = 3$).

(I) Assessment of respiration in tumor-derived cell lines using Seahorse analysis ($n \geq 3$).

(J) Detection of ATP levels in different tumor-derived cell lines ($n = 3$).

(K) Restoration of tumor forming efficacy in cells derived from B16 ρ^0 tumors from Miro1^{KO} and Ctrl mice $n = 5$. Paired t test with Gaussian distribution (C, separately for each day), one-way ANOVA with Dunnett's multiple comparisons test (D–F, I), Sidak test (J) or unpaired t test (D–F, I for comparison of B16 and B16 ρ^0 cells).

Data are presented as mean values \pm SEM. * $p < 0.05$, ** $p < 0.01$, *** $p < 0.001$, **** $p < 0.0001$. ns, not significant. See also Figure S2.

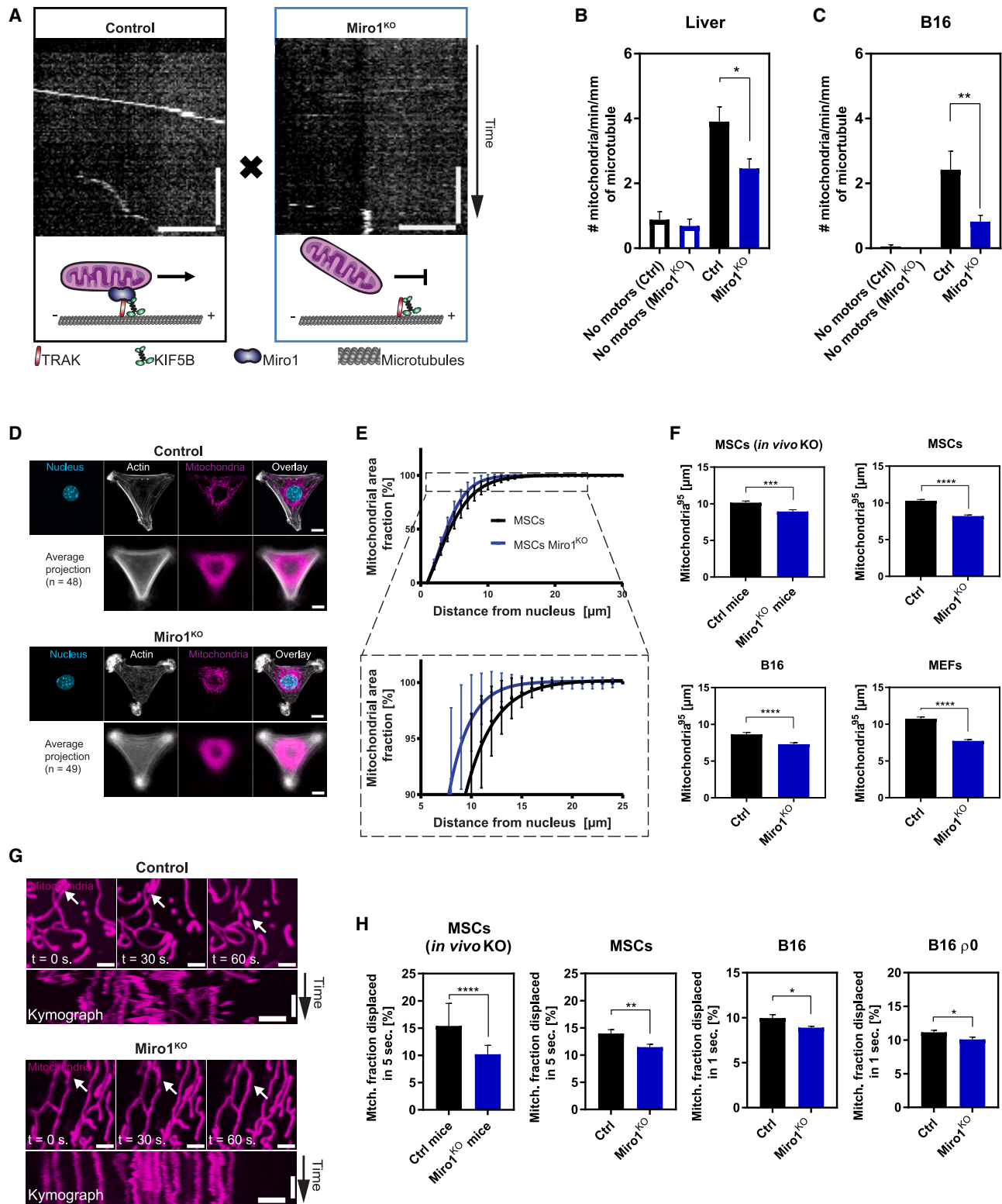


Figure 3. Miro1 depletion impairs movement of mitochondria and alters mitochondrial network

(A) Kymograph from time-lapse imaging with interference reflectance microscopy of the *in vitro* reconstituted system. Mitochondria (represented by bright lines) from Ctrl or Miro1^{KO} cells associate with microtubules and move along them. Horizontal scale bar, 3 μm ; vertical scale bar, 30 s. Below, a scheme of the reconstituted system.

(legend continued on next page)

We next analyzed the effects of the absence of Miro1 on dynamics of the mitochondrial network. We adopted the previously described methodology and quantified displacement of mitochondria based on changes in organelle localization over subsequent time points.³⁸ In MSCs, B16, and B16 ρ^0 cells, the absence of Miro1 resulted in a significant reduction in mitochondrial mobility (Figures 3G and 3H). This reduction was due to decreased microtubule-mediated movement, which was confirmed by a strong effect of the microtubule inhibitor nocodazole, while the actin inhibitor cytochalasin D had little or no effect (Figure S3E). Both static snapshots of mitochondrial network in subsequent timepoints (Figure 3G, top) as well as kymographs capturing mitochondrial mobility within a 5-min period (Figure 3G, bottom) illustrate reduced mitochondrial dynamics in Miro1^{KO} cells.

Taken together, these findings demonstrate that Miro1 plays an important role in the association of mitochondria with the adaptor and motor proteins, enabling their movement along microtubules. At the cellular level, Miro1 governs the dynamics of the mitochondrial network and, importantly, secures the mitochondrial distribution toward the cell membrane.

Mitochondria are transferred via TNTs and their movement is modulated by Miro1

To detect mitochondrial transfer *in vitro*, we used two different co-culture approaches (Figure 4A). First, we used a custom-made microfluidic device (Figure S4A), allowing spatially separated seeding of B16 ρ^0 GFP cells and MSCs harboring fluorescently labeled mitochondria (either mito::mKate2 or MitoTracker DeepRed). This approach allowed us to identify relatively rare events of mitochondrial transfer from MSCs to B16 ρ^0 cells (Figure S4B) and direct connection of these cells by TNTs containing mitochondria (Figure 4B).

To obtain evidence of mitochondrial transfer in mouse tumors, we initiated tumor formation by grafting B16 ρ^0 GFP cells into mito::mKate2 mice (Figure 2A). We harvested tumors shortly after grafting of cancer cells (D5 and D10) and analyzed these tumor samples using microscopy (Figure 4A). Within 24 h after harvesting, we detected formation of TNT connections between cancer and stromal cells accompanied by acquisition of stromal cell-derived mitochondria by cancer cells (Figure 4C). We also observed that GFP-positive cancer cells contain mKate2-positive mitochondria of stromal origin, persisting for at least another 24 h (Figures 4D and S4C).

We next investigated the potential impact of Miro1 on the presence of mitochondria within TNTs. To achieve this, we

used monoculture of MSCs known to frequently form intercellular connections that facilitate mitochondrial transfer (Figure 4E). The high number of TNTs makes it possible to quantitatively assess the effect of Miro1 on the presence of mitochondria within these structures. The number of mitochondria in TNTs considerably decreased after deletion of Miro1 (Figure 4E). We also inspected the ultrastructure of TNTs transferring mitochondria using correlative light and electron microscopy (Figure S4D), which revealed the presence of several mitochondria transferred via a single TNT containing microtubules, further supporting the mechanism of mitochondrial transport by means of these structures (Figures 4F and 4G).

Overall, our findings provide evidence of the mechanism of HMT both in an *in vitro* co-culture system and within the complex tumor microenvironment, highlighting the significance of TNT-mediated mitochondrial exchange between stromal and cancer cells and the role of Miro1 in modulating this process.

DISCUSSION

Despite metabolic remodeling of cancer cells in favor of glycolysis over OXPHOS in the presence of oxygen, so-called aerobic glycolysis, the importance of mitochondrial metabolism in cancer initiation, progression, and adaptation is well established.^{4,65,66} Mitochondria are critically involved in regulating cellular metabolism as well as actively participating in the fate of cancer cells toward diverse bioenergetic pathways, resulting in their adaptation to various environmental cues. Notably, radiation therapy and chemotherapy can induce mtDNA mutations.^{67–69} Mutations in mtDNA^{25,70–72} or genetic ablation of OXPHOS in cancer cells^{13,14} affect tumor formation and may lead to the acquisition of oxidatively active mitochondria from nearby stromal cells.^{20,25,29,33,67}

We hypothesized that deletion of the adaptor protein Miro1 responsible for microtubular movement of mitochondria would impair transfer of mitochondria between tumor stroma and ρ^0 cancer cells, ultimately leading to inhibition of tumor formation. We detected a significantly lower tumor growth when B16 ρ^0 or HcMel12 ρ^0 cells were grafted in Miro1^{KO} mice compared with the Ctrl group. Using Miro1^{KO} mito::mKate2 mice and B16 ρ^0 GFP cells, we confirmed impaired mitochondrial transfer at early time points of tumor development. Importantly, we demonstrated that these differences were not due to impaired bioenergetics of the donated mitochondria. These results are consistent with *in vitro* studies pointing to involvement of Miro1 in HMT in

(B and C) Quantification of landing rate of mitochondria to microtubules isolated from (B) liver of Ctrl and Miro1^{KO} mice and (C) B16 cells. The system without motor and adaptor proteins was used as a Ctrl, $n \geq 3$ fields of view per each group per experiment ($n = 3$).

(D–F) Positioning of mitochondria in Ctrl and Miro1^{KO} cells. (D) Visualization of mitochondrial network using micropatterned chips. MitoTracker DeepRed (magenta, mitochondria), Alexa Fluor 488 phalloidin (white, actin), and Hoechst 33342 (blue, nucleus) Representative images of Ctrl and Miro1^{KO} MSCs with corresponding average intensity projections of analyzed cells. Scale bar, 10 μm . (E) Quantification of cumulative mitochondrial area fraction in shells radiating from the nucleus toward the periphery of the cell with Sholl-based analysis ($n \geq 90$). (F) Mito95 value (diameter of the perinuclear area containing 95% of the mitochondrial network) of MSCs with Miro1^{KO} induced *in vitro* or isolated from Miro1^{KO} mice ($n \geq 90$), MEFs ($n \geq 90$), and B16 cells ($n \geq 35$) (B16/2 separate clones of Miro1^{KO}).

(G and H) Miro1^{KO} impedes movement of mitochondria within the cells. (Top) Illustrative images (static snapshots) of the mitochondrial network in MSCs (Ctrl vs. Miro1^{KO}) at 30-s intervals; scale bar, 2 μm . (Bottom) kymographs capturing the movement of mitochondria during 5 min of timelapse imaging. Horizontal scale bar, 5 μm ; vertical scale, bar 120 s. (H) Quantification of mitochondrial movement, $n = 2$, $n \geq 10$ FOV for each experiment and clone (B16/2 separate clones of Miro1^{KO}). Unpaired t test (F, H), one-way ANOVA with Tukey multiple comparison test (C).

Data are presented as mean values \pm SEM. * $p < 0.05$, ** $p < 0.01$, *** $p < 0.001$, **** $p < 0.0001$. ns, not significant. See also Figure S3.

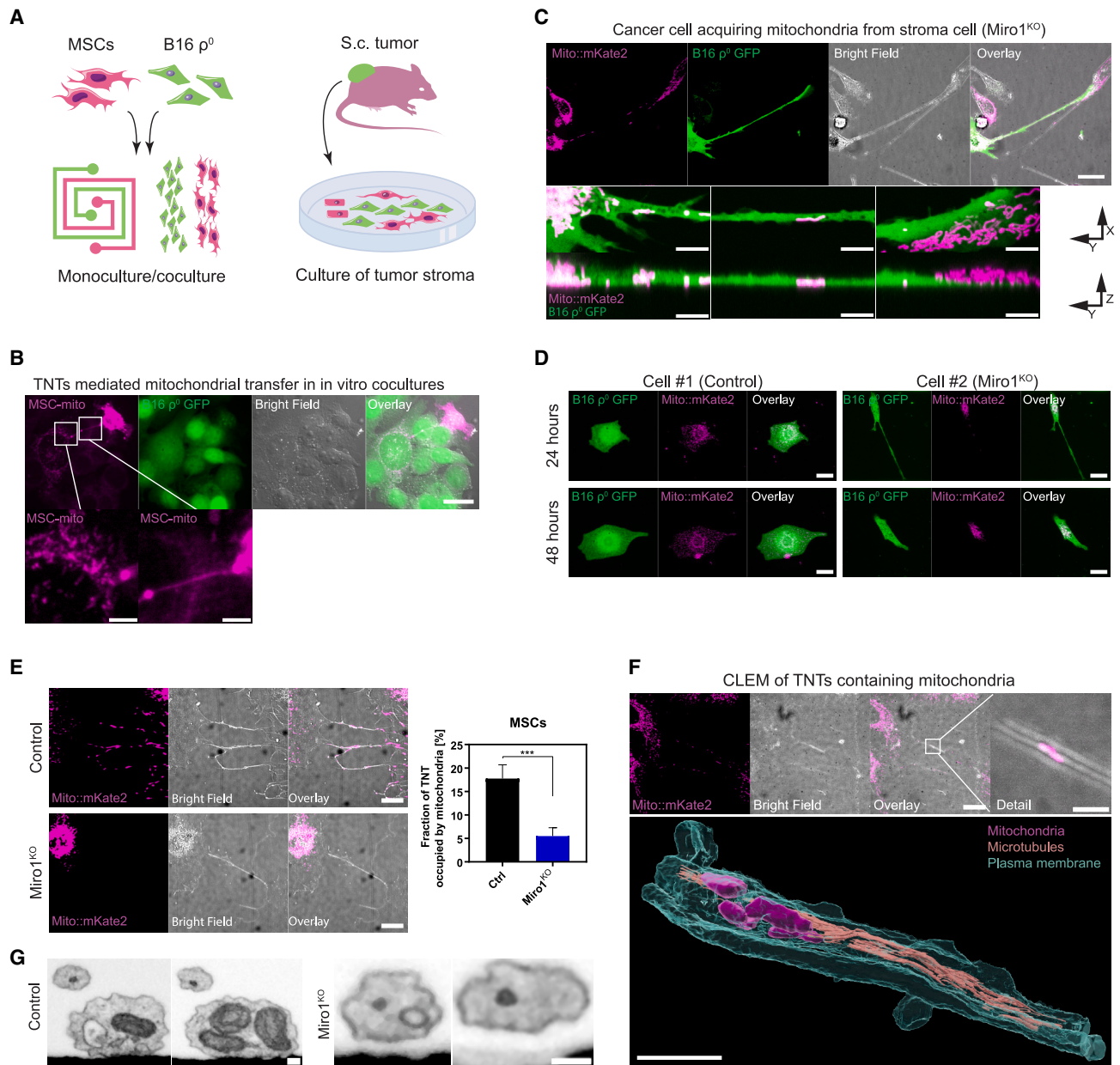


Figure 4. Mitochondria are transferred via TNTs and their movement is regulated by Miro1

(A) Schematic illustration of the experimental approach

(B) Mitochondrial transfer captured in *in vitro* co-cultures in microfluidic device. MSCs were labeled with MitoTracker DeepRed (magenta) and cocultured with B16 p⁰ GFP cancer cells (green). Mitochondria were transferred via TNTs from MSC to cancer cell. Scale bars, 25 μ m and 5 μ m (magnified images).

(C and D) Mitochondrial transfer via TNTs in tumor samples. (C) Ctrl and Miro1^{KO} mice, both mito::mKate2 (magenta), were grafted with B16 p⁰ GFP cells (green). Tumors were dissected at different time points as depicted in Figure 2A; D5 is shown here. Scale bar, 25 μ m. (Bottom) Cross-sections of a TNT containing mitochondria originating from tumor stromal cells, day 10 is shown here. Scale bars, 5 μ m. (D) B16 p⁰ GFP cancer cells containing mKate2-positive mitochondria acquired from tumor stromal cells, day 10 is shown here. Scale bars, 10 μ m.

(E) Miro1^{KO} decreases the frequency of mitochondria transferred via TNTs formed by MSCs. (Left) TNTs transferring mitochondria in monocultures of Ctrl or Miro1^{KO} MSCs, scale bar, 25 μ m. (Right) Quantification, $n = 2$ biological replicates, unpaired t test, $n = 40$ cells. Data are presented as mean values \pm SEM. * $p < 0.05$, ** $p < 0.01$, *** $p < 0.001$, **** $p < 0.0001$.

(F) Ultrastructure of selected TNTs transferring mitochondria between two Ctrl MSCs. Scale bar, 25 μ m and 3 μ m (detail). Below, 3D reconstruction of corresponding part of TNT transferring mitochondria along microtubules imaged with FIB-SEM. Scale bar, 1 μ m.

(G) Cross-sections of TNTs connecting Ctrl or Miro1^{KO} MSCs imaged with FIB-SEM. The TNT connecting Ctrl MSCs (left) contains mitochondria in contrast with empty TNT from Miro1^{KO}. Scale bar, 0.1 μ m. See also Figure S4.

cancer and other disease models.^{73–78} We did not observe significant differences in mitochondrial transfer between Ctrl and Miro1^{KO} group after day 15, likely due to several reasons. While mKate2 is stable, its half-life is limited after being transferred to recipient cells and its signal could be diluted in the mitochondrial process of fusion-fission. Importantly, HMT is an energy-intensive process, suggesting that mitochondrial transfer may occur only until recipient cells reach a threshold for replenishing organelles needed to replicate their own mtDNA, which was reached sooner in the Ctrl samples than in the KOs. In our previous work, we demonstrated that in breast cancer 4T1 ρ^0 cells, mitochondrial complexes and respiration were fully restored by day 15 compared with parental cells.³² These data align with our observations for B16 ρ^0 cells. We further explored functional consequences of impaired HMT in Miro1^{KO} mice. Here, we show that impaired HMT at initial stages of tumor development resulted in delay in acquisition of mtDNA and the ensuing recovery of respiration, proliferation and tumor-forming capacity when cell lines were derived from B16 ρ^0 (D5–D20 sublines) tumors that developed in Miro1^{KO} mice.

Our data demonstrate a regulatory role of Miro1 in HMT in early time-points of cancer development in the orthotopic melanoma model. The lack of complete inhibition of HMT could be explained by the possible participation of the Miro2 protein in this process. Although both proteins facilitate the movement of mitochondria along the actin and tubulin cytoskeleton, developmental studies have indicated that Miro2 cannot fully compensate for the loss of Miro1, while homozygotic deletion of Miro1 is embryonically lethal,^{38,55} supporting the dominant role of Miro1. Furthermore, *in vitro* studies revealed some residual mitochondrial movement in the absence of these two proteins while in lower metazoans additional proteins have been reported as adaptors facilitating mitochondrial movement.^{38,79} We observed no Miro2 overexpression in Miro1^{KO} cells in both non-cancerous cells and B16 cancer cells (data not shown) and we detected very rare instances of mitochondrial transfer in B16 ρ^0 tumors isolated from Miro1^{KO} mice, even at early time points, suggesting the following scenario. Even though Miro2 and other unidentified proteins cannot fully compensate for Miro1 loss, they may facilitate HMT at a significantly reduced rate, resulting in a prolonged time needed to replenish mitochondrial levels.

We demonstrated that, regardless of the partial impact of Miro1 deletion on proliferation of several clones of B16 and B16 ρ^0 cells,^{60,80} the deletion of Miro1 alone in recipient cancer cells did not affect tumor growth in the mouse model, suggesting no crucial function of Miro1 in HMT in recipient cells. Importantly, we observed that Miro1^{KO} in B16 ρ^0 cells had no additional impact on the mitochondrial network and a non-significant effect on the landing rate of mitochondria on microtubules suggesting that these features are already altered to some extent in ρ^0 , which may obscure the *in vivo* effect of Miro1^{KO} in recipient B16 ρ^0 cells.

The question of how Miro1 is connected to HMT remains open. As mentioned above, TNTs are the most prevalent means for HMT composed of actin filaments serving primarily as structural elements, and of microtubules being responsible for HMT, allowing for movement of organelles and other cargo.^{21,81,82} To investigate whether microtubule-based transport is altered in

Miro1-depleted cells, we used a reconstituted system involving mitochondria, adaptor and motor proteins, and microtubules.^{62,63} This system allowed us to exclude potential effects of other molecular motors (e.g., myosins). Our results demonstrate a decrease in the frequency of microtubule transport of mitochondria from both cells and tissues with Miro1^{KO}. These data, together with the overall reduced mitochondrial movement, underscore the primary role of microtubule-mediated transport facilitated by Miro1. Our findings are consistent with published data highlighting the dominant role of Miro1 in tubulin-based transport.³⁸ Finally, we have identified HMT and TNTs transporting mitochondria and provided insight into the morphology of these structures *in vitro* in a co-culture system of B16 ρ^0 GFP cells and MSCs as well as in tumors samples of B16 ρ^0 GFP cells. We have also indirectly (in MSCs monoculture) shown that Miro1^{KO} status impacts the number of mitochondria within TNTs. It is not unreasonable to anticipate similar effects in the transport of healthy mitochondria from donors to other respiration-incompetent cancer cells.

Although TNTs are a well-documented mechanism for inter-cellular transport and are extensively supported by the literature, their investigation has predominantly been limited to *in vitro* conditions. As documented in our recent work¹⁷ and elsewhere,^{19,20} other mechanisms of HMT have been identified in relation to various mitochondria-related diseases. Besides TNTs, cell fusion, the formation of cell-cell junctions, and extracellular vesicles (EVs) have all been implicated in the HMT process. Furthermore, our research has revealed that Miro1 modulates HMT during the wound-healing process promoted by MSCs (unpublished data). This process is mediated by clathrin-dependent transfer of mitochondria via EVs from platelets to MSCs.⁸³ Miro1 may influence the formation of mitochondrial-derived vesicles,⁸⁴ but this is highly specific to its location in the mitochondrial membrane. The resulting effect of Miro1^{KO} on EV-dependent mitochondrial transport might be attributed to disruption of the mitochondrial network and altered mitochondrial localization, hindering their ability to reach the plasma membrane and be transported via both TNTs and EVs.⁸⁴ While the current literature on HMT in cancer and our work primarily focuses on studies centered around TNT formation, we cannot exclude the possibility of involvement of other means of mitochondrial transport. Several investigations have demonstrated the transfer of mtDNA^{27,85} and mitochondria⁸⁶ via the formation of EVs. These studies indicate that HMT plays another crucial role: enhancing the metastatic potential of cancer cells. This dual function highlights the complexity of HMT involvement in cancer biology, suggesting that it may contribute to both tumor growth and the ability of cancer cells to spread to distant sites within the body. Nevertheless, in the case of HMT occurring to enhance the metastatic capabilities of cells, this pertains to later stages of tumor growth, rather than the initial stages, in comparison with our HMT model using ρ^0 cells, where mitochondrial transfer occurs to restore cancer cell proliferation.

While mutations in the *RHOT1* gene are more commonly linked to neurological disorders such as Parkinson's and Alzheimer's diseases, the exploration of *RHOT1* mutations in cancer is an emerging field.^{40,54} Since *RHOT1* plays a key role in regulating mitochondrial dynamics, its mutations or

dysregulation may contribute to cancer development by disrupting critical mitochondrial functions such as mitochondrial trafficking, energy distribution, and cellular stress responses. Here, we describe an additional role for *RHOT1* (Miro1 protein) in specifically regulating the transfer of whole mitochondria to melanoma cancer cells, driving their proliferation, and enhancing their fitness and ability to survive under stressful conditions. *RHOT1* is altered in approximately 0.23% of all cancers, and while these alterations are rare, they have been detected in specific cancer types, including lung, colon, pancreatic adenocarcinoma, and breast cancers.⁸⁷ Several studies have identified overexpression of *RHOT1*/Miro1 or its circRNA in various types of cancer^{45–51} correlating with poor prognosis,⁴⁸ increased proliferation, invasion, and metastasis.^{45,46,48,50,51} While there are currently no clinical trials specifically targeting the *RHOT1* gene or its product, Miro1, in either neurological diseases or cancer, recent advances show promise.^{88,89} One notable compound, known as the Miro1 reducer, has been shown to effectively reduce Miro1 levels in fibroblasts derived from patients with Parkinson's disease and *in vivo* in fly models, reducing stress-induced degeneration of dopaminergic neurons and locomotor deficits, respectively.⁸⁸ Future studies could investigate whether this compound inhibits growth or metastasis of specific cancer types. A more effective therapeutic approach may involve interventions targeting mitochondrial trafficking by nocodazole, a microtubule-depolymerizing agent, that has been shown to induce cell-cycle arrest and apoptosis in multiple myeloma cells.⁹⁰ A potential combination of Miro1 inhibitors or nocodazole with other drugs targeting mitochondrial metabolism, such as metformin⁹¹ or atovaquone,⁹² could be promising. However, the possible side effects on the hematopoietic and immune systems must be carefully evaluated.

To summarize, we have demonstrated that Miro1^{KO} within the tumor stroma of melanoma modulates growth of tumors derived from B16 ρ^0 and HcMel12 ρ^0 cells. We showed that the lag and kinetics of tumor formation by B16 ρ^0 at early time points of tumor development are affected by reduced frequency of mitochondrial transfer from tumor stromal cells to cancer cells. Our research also shows that HMT in the B16 melanoma model occurs via TNTs, defining the function of Miro1 adaptor protein and the microtubular mobility system in the process.

Limitations of the study

We demonstrate that Miro1 regulates tumor formation in ρ^0 melanoma cells during initial stages of tumor development. Lack of complete inhibition of HMT in Miro1^{KO} mice could be due to the effect of Miro2 or other yet unidentified adaptor protein transporting mitochondria, which remain unresolved. Although we observed TNT formation in our experimental model, this may be closely tied to *in vitro* conditions. We also did not investigate other means of HMT and thus cannot exclude other processes occurring alongside TNT formation. Additionally, while we observed no effect of HMT on B16 tumor growth, we cannot exclude difference in growth of the HcMel12 cell line in Ctrl and Miro1^{KO} mice resulted in impaired mitochondrial transfer that could be important for this particular cell line even in the presence of respiration-competent mitochondria.

RESOURCE AVAILABILITY

Lead contact

Further information and requests for reagents may be directed and will be fulfilled by the lead contact, Jiri Neuzil (j.neuzil@griffith.edu.au).

Materials availability

All biological materials from this study are available from the [lead contact](#) upon request or commercial sources.

Data and code availability

- Data reported in this paper will be shared by the [lead contact](#) upon request.
- Original code for the Sholl analysis of mitochondria in Fiji has been deposited at Mendeley Data and is publicly available as of the date of publication. The DOI is listed in the [key resources table](#).
- All other items: any additional information required to reanalyze the data reported in this paper is available from the [lead contact](#) upon request.

ACKNOWLEDGMENTS

This work was supported by BIOCEV European Regional Development Fund CZ.1.05/1.100/02.0109 and Institute of Biotechnology RVO 86652036, by grant from the Czech Science Foundation GA21-04607X and 20-05942S to J.Neuzil, GA23-05303S to S.B., GF24-10406K to R.Z., GA22-34507S to J.R., by a grant from the Ministry of Health of the Czech Republic NU23-03-00226 to S.D., by Grant Agency of Charles University GA UK 320922 to J.Novak, GA UK 408222 to P.B., GA UK 1242120 to M.Dubisova, by FCT PhD Studentship 2020.04765.BD to G.O., by grant CRUK SI Core Funding (A31287, A_BICR_1920_Gammage) to C.M.C. and P.A.G. The authors used services of Imaging methods core facility at Faculty of Science of Charles University in Biocev supported by the project LM2023050 Czech-Biolmaging (MEYS CZ), LM2018129 Czech-Biolmaging (MEYS CZ) to Z.N. and J.Novak., and Czech Centre for Phenogenomics (IMG, CAS CZ) supported by the Czech Academy of Sciences RVO 68378050 and LM2023036 (MEYS CZ).

AUTHOR CONTRIBUTIONS

Conceptualization: J.Neuzil, Z.N., J.Novak, and J.R. Writing original draft, review & editing: Z.N., J.Novak, and J.Neuzil. Experimental work, methodology, and editing: Z.N., J.Novak, G.L.O., J.L., P.B., M.Dubisova, S.D., S.M., M.Da-lecka, C.M.C., V.P., L.G., L.S., J.P., D.S., S.M.N., D.P.R., G.L.D., R.Z., R.S., P.A.G., M.G.T., Z.L., J.K., P.J.O., H.J.D., M.V.B., A.M.R., S.B., and J.R.

DECLARATION OF INTERESTS

The authors declare no competing interests.

DECLARATION OF GENERATIVE AI AND AI-ASSISTED TECHNOLOGIES IN THE WRITING PROCESS

ChatGPT was used for grammar and vocabulary purposes.

STAR★METHODS

Detailed methods are provided in the online version of this paper and include the following:

- [KEY RESOURCES TABLE](#)
- [EXPERIMENTAL MODEL AND STUDY PARTICIPANT DETAILS](#)
 - Cell culture
 - Animal models
 - Hematology analysis
 - Biochemistry analysis
 - Indirect calorimetry
- [METHOD DETAILS](#)
 - Genotyping of mice

- Western blotting
- Native blue gel electrophoresis (NBGE)
- Crystal violet assay
- High resolution respirometry
- Seahorse measurements
- ATP concentration evaluation
- Detection of mitochondrial mass by fluorescent cytometry
- Mitochondrial membrane potential evaluation
- qPCR
- Measurement of mtDNA copy number
- Quantification of mtDNA nucleoids
- *In vivo* experiments
- Imaging of tumor sections and analysis of mitochondrial transfer
- Isolation of mitochondria
- TUNEL assay
- Analysis of mitochondrial positioning using CYTOO chips
- Analysis of mitochondrial network dynamics
- Quantification of mitochondrial movement in cell-free reconstituted system
- Correlative light and electron microscopy
- Transmission electron microscopy
- Microfluidic co-cultures of cells
- Analysis of mitochondrial presence in TNTs of MSCs
- Scheme design
- **QUANTIFICATION AND STATISTICAL ANALYSIS**

SUPPLEMENTAL INFORMATION

Supplemental information can be found online at <https://doi.org/10.1016/j.celrep.2024.115154>.

Received: January 22, 2024

Revised: October 31, 2024

Accepted: December 13, 2024

Published: January 9, 2025

REFERENCES

1. Bray, F., Laversanne, M., Weiderpass, E., and Soerjomataram, I. (2021). The ever-increasing importance of cancer as a leading cause of premature death worldwide. *Cancer* 127, 3029–3030. <https://doi.org/10.1002/ncr.33587>.
2. Miller, K.D., Nogueira, L., Devasia, T., Mariotto, A.B., Yabroff, K.R., Jemal, A., Kramer, J., and Siegel, R.L. (2022). Cancer treatment and survivorship statistics, 2022. *CA A Cancer J. Clin.* 72, 409–436. <https://doi.org/10.3322/caac.21731>.
3. DeBerardinis, R.J., and Chandel, N.S. (2020). We need to talk about the Warburg effect. *Nat. Metab.* 2, 127–129. <https://doi.org/10.1038/s42255-020-0172-2>.
4. Koppenol, W.H., Bounds, P.L., and Dang, C.V. (2011). Otto Warburg's contributions to current concepts of cancer metabolism. *Nat. Rev. Cancer* 11, 325–337. <https://doi.org/10.1038/nrc3038>.
5. Warburg, O. (1956). On the origin of cancer cells. *Science* 123, 309–314. <https://doi.org/10.1126/science.123.3191.309>.
6. Lanzetti, L. (2024). Oncometabolites at the crossroads of genetic, epigenetic and ecological alterations in cancer. *Cell Death Differ.* 31, 1582–1594. <https://doi.org/10.1038/s41418-024-01402-6>.
7. Chen, J., Cui, L., Lu, S., and Xu, S. (2024). Amino acid metabolism in tumor biology and therapy. *Cell Death Dis.* 15, 42. <https://doi.org/10.1038/s41419-024-06435-w>.
8. Pavlova, N.N., and Thompson, C.B. (2016). The Emerging Hallmarks of Cancer Metabolism. *Cell Metabol.* 23, 27–47. <https://doi.org/10.1016/j.cmet.2015.12.006>.
9. Wang, J.B., Erickson, J.W., Fuji, R., Ramachandran, S., Gao, P., Dinavahi, R., Wilson, K.F., Ambrosio, A.L.B., Dias, S.M.G., Dang, C.V., and Cerione, R.A. (2010). Targeting mitochondrial glutaminase activity inhibits oncogenic transformation. *Cancer. Cell.* 18, 207–219. <https://doi.org/10.1016/j.ccr.2010.08.009>.
10. Zhang, M., Di Martino, J.S., Bowman, R.L., Campbell, N.R., Baksh, S.C., Simon-Vermot, T., Kim, I.S., Haldeman, P., Mondal, C., Yong-Gonzales, V., et al. (2018). Adipocyte-Derived Lipids Mediate Melanoma Progression via FATP Proteins. *Cancer Discov.* 8, 1006–1025. <https://doi.org/10.1158/2159-8290.CD-17-1371>.
11. Hanai, J.I., Doro, N., Sasaki, A.T., Kobayashi, S., Cantley, L.C., Seth, P., and Sukhatme, V.P. (2012). Inhibition of lung cancer growth: ATP citrate lyase knockdown and statin treatment leads to dual blockade of mitogen-activated protein kinase (MAPK) and phosphatidylinositol-3-kinase (PI3K)/AKT pathways. *J. Cell. Physiol.* 227, 1709–1720. <https://doi.org/10.1002/jcp.22895>.
12. Sullivan, L.B., Gui, D.Y., Hosios, A.M., Bush, L.N., Freinkman, E., and Vander Heiden, M.G. (2015). Supporting Aspartate Biosynthesis Is an Essential Function of Respiration in Proliferating Cells. *Cell* 162, 552–563. <https://doi.org/10.1016/j.cell.2015.07.017>.
13. Viale, A., Pettazoni, P., Lyssiotis, C.A., Ying, H., Sánchez, N., Marchesini, M., Carugo, A., Green, T., Seth, S., Giuliani, V., et al. (2014). Oncogene ablation-resistant pancreatic cancer cells depend on mitochondrial function. *Nature* 514, 628–632. <https://doi.org/10.1038/nature13611>.
14. Weinberg, F., Hamanaka, R., Wheaton, W.W., Weinberg, S., Joseph, J., Lopez, M., Kalyanaraman, B., Mutlu, G.M., Budinger, G.R.S., and Chandel, N.S. (2010). Mitochondrial metabolism and ROS generation are essential for Kras-mediated tumorigenicity. *Proc. Natl. Acad. Sci. USA* 107, 8788–8793. <https://doi.org/10.1073/pnas.1003428107>.
15. Oliveira, G.L., Coelho, A.R., Marques, R., and Oliveira, P.J. (2021). Cancer cell metabolism: Rewiring the mitochondrial hub. *Biochim. Biophys. Acta, Mol. Basis Dis.* 1867, 166016. <https://doi.org/10.1016/j.bbadis.2020.166016>.
16. Neuzil, J., Dong, L.F., Rohlena, J., Truksa, J., and Ralph, S.J. (2013). Classification of mitocans, anti-cancer drugs acting on mitochondria. *Mitochondrion* 13, 199–208. <https://doi.org/10.1016/j.mito.2012.07.112>.
17. Dong, L.F., Rohlena, J., Zobalova, R., Nahacka, Z., Rodriguez, A.M., Berridge, M.V., and Neuzil, J. (2023). Mitochondria on the move: Horizontal mitochondrial transfer in disease and health. *J. Cell Biol.* 222, e202211044. <https://doi.org/10.1083/jcb.202211044>.
18. Berridge, M.V., Dong, L., and Neuzil, J. (2015). Mitochondrial DNA in Tumor Initiation, Progression, and Metastasis: Role of Horizontal mtDNA Transfer. *Cancer Res.* 75, 3203–3208. <https://doi.org/10.1158/0008-5472.CAN-15-0859>.
19. Borcherding, N., and Brestoff, J.R. (2023). The power and potential of mitochondria transfer. *Nature* 623, 283–291. <https://doi.org/10.1038/s41586-023-06537-z>.
20. Zampieri, L.X., Silva-Almeida, C., Rondeau, J.D., and Sonveaux, P. (2021). Mitochondrial Transfer in Cancer: A Comprehensive Review. *Int. J. Mol. Sci.* 22, 3245. <https://doi.org/10.3390/ijms22063245>.
21. Rustom, A., Saffrich, R., Markovic, I., Walther, P., and Gerdes, H.H. (2004). Nanotubular highways for intercellular organelle transport. *Science* 303, 1007–1010. <https://doi.org/10.1126/science.1093133>.
22. Koyanagi, M., Brandes, R.P., Haendeler, J., Zeiher, A.M., and Dimmeler, S. (2005). Cell-to-cell connection of endothelial progenitor cells with cardiac myocytes by nanotubes: a novel mechanism for cell fate changes? *Circ. Res.* 96, 1039–1041. <https://doi.org/10.1161/01.RES.0000168650.23479.0c>.
23. Spees, J.L., Olson, S.D., Whitney, M.J., and Prockop, D.J. (2006). Mitochondrial transfer between cells can rescue aerobic respiration. *Proc. Natl. Acad. Sci. USA* 103, 1283–1288. <https://doi.org/10.1073/pnas.0510511103>.
24. Cho, Y.M., Kim, J.H., Kim, M., Park, S.J., Koh, S.H., Ahn, H.S., Kang, G.H., Lee, J.B., Park, K.S., and Lee, H.K. (2012). Mesenchymal stem cells transfer mitochondria to the cells with virtually no mitochondrial function

- but not with pathogenic mtDNA mutations. *PLoS One* 7, e32778. <https://doi.org/10.1371/journal.pone.0032778>.
25. Moschoi, R., Imbert, V., Nebout, M., Chiche, J., Mary, D., Prebet, T., Saland, E., Castellano, R., Pouyet, L., Collette, Y., et al. (2016). Protective mitochondrial transfer from bone marrow stromal cells to acute myeloid leukemic cells during chemotherapy. *Blood* 128, 253–264. <https://doi.org/10.1182/blood-2015-07-655860>.
 26. Lu, J., Zheng, X., Li, F., Yu, Y., Chen, Z., Liu, Z., Wang, Z., Xu, H., and Yang, W. (2017). Tunneling nanotubes promote intercellular mitochondria transfer followed by increased invasiveness in bladder cancer cells. *Oncotarget* 8, 15539–15552. <https://doi.org/10.18632/oncotarget.14695>.
 27. Takenaga, K., Koshikawa, N., and Nagase, H. (2021). Intercellular transfer of mitochondrial DNA carrying metastasis-enhancing pathogenic mutations from high- to low-metastatic tumor cells and stromal cells via extracellular vesicles. *BMC Mol. Cell Biol.* 22, 52. <https://doi.org/10.1186/s12860-021-00391-5>.
 28. Valdebenito, S., Malik, S., Luu, R., Loudig, O., Mitchell, M., Okafo, G., Bhat, K., Pridaux, B., and Eugenin, E.A. (2021). Tunneling nanotubes, TNT, communicate glioblastoma with surrounding non-tumor astrocytes to adapt them to hypoxic and metabolic tumor conditions. *Sci. Rep.* 11, 14556. <https://doi.org/10.1038/s41598-021-93775-8>.
 29. Dong, L.F., Kovarova, J., Bajzikova, M., Bezawork-Geleta, A., Svec, D., Endaya, B., Sachaphibulkij, K., Coelho, A.R., Sebkova, N., Ruzickova, A., et al. (2017). Horizontal transfer of whole mitochondria restores tumorigenic potential in mitochondrial DNA-deficient cancer cells. *Elife* 6, e22187. <https://doi.org/10.7554/eLife.22187>.
 30. Wang, J., Liu, X., Qiu, Y., Shi, Y., Cai, J., Wang, B., Wei, X., Ke, Q., Sui, X., Wang, Y., et al. (2018). Cell adhesion-mediated mitochondria transfer contributes to mesenchymal stem cell-induced chemoresistance on T cell acute lymphoblastic leukemia cells. *J. Hematol. Oncol.* 11, 11. <https://doi.org/10.1186/s13045-018-0554-z>.
 31. Burt, R., Dey, A., Aref, S., Aguiar, M., Akarca, A., Bailey, K., Day, W., Hooper, S., Kirkwood, A., Kirschner, K., et al. (2019). Activated stromal cells transfer mitochondria to rescue acute lymphoblastic leukemia cells from oxidative stress. *Blood* 134, 1415–1429. <https://doi.org/10.1182/blood.2019001398>.
 32. Bajzikova, M., Kovarova, J., Coelho, A.R., Boukalova, S., Oh, S., Rohlenova, K., Svec, D., Hubackova, S., Endaya, B., Judasova, K., et al. (2019). Reactivation of Dihydroorotate Dehydrogenase-Driven Pyrimidine Biosynthesis Restores Tumor Growth of Respiration-Deficient Cancer Cells. *Cell Metabol.* 29, 399–416.e10. <https://doi.org/10.1016/j.cmet.2018.10.014>.
 33. Tan, A.S., Baty, J.W., Dong, L.F., Bezawork-Geleta, A., Endaya, B., Goodwin, J., Bajzikova, M., Kovarova, J., Peterka, M., Yan, B., et al. (2015). Mitochondrial genome acquisition restores respiratory function and tumorigenic potential of cancer cells without mitochondrial DNA. *Cell Metabol.* 21, 81–94. <https://doi.org/10.1016/j.cmet.2014.12.003>.
 34. Osswald, M., Jung, E., Sahm, F., Solecki, G., Venkataramani, V., Blaes, J., Weil, S., Horstmann, H., Wiestler, B., Syed, M., et al. (2015). Brain tumour cells interconnect to a functional and resistant network. *Nature* 528, 93–98. <https://doi.org/10.1038/nature16071>.
 35. Cordero Cervantes, D., and Zurzolo, C. (2021). Peering into tunneling nanotubes-The path forward. *EMBO J.* 40, e105789. <https://doi.org/10.15252/embj.2020105789>.
 36. Raghavan, A., Rao, P., Neuzil, J., Pountney, D.L., and Nath, S. (2021). Oxidative stress and Rho GTPases in the biogenesis of tunnelling nanotubes: implications in disease and therapy. *Cell. Mol. Life Sci.* 79, 36. <https://doi.org/10.1007/s00018-021-04040-0>.
 37. MacAskill, A.F., and Kittler, J.T. (2010). Control of mitochondrial transport and localization in neurons. *Trends Cell Biol.* 20, 102–112. <https://doi.org/10.1016/j.tcb.2009.11.002>.
 38. López-Domenech, G., Covill-Cooke, C., Ivankovic, D., Half, E.F., Sheehan, D.F., Norkett, R., Birs, N., and Kittler, J.T. (2018). Miro proteins coordinate microtubule- and actin-dependent mitochondrial transport and distribution. *EMBO J.* 37, 321–336. <https://doi.org/10.15252/embj.201696380>.
 39. Nahacka, Z., Zabalova, R., Dubisova, M., Rohlena, J., and Neuzil, J. (2021). Miro proteins connect mitochondrial function and intercellular transport. *Crit. Rev. Biochem. Mol. Biol.* 56, 401–425. <https://doi.org/10.1080/10409238.2021.1925216>.
 40. Eberhardt, E.L., Ludlam, A.V., Tan, Z., and Cianfrocco, M.A. (2020). Miro: A molecular switch at the center of mitochondrial regulation. *Protein Sci.* 29, 1269–1284. <https://doi.org/10.1002/pro.3839>.
 41. Fransson, S., Ruusala, A., and Aspenström, P. (2006). The atypical Rho GTPases Miro-1 and Miro-2 have essential roles in mitochondrial trafficking. *Biochem. Biophys. Res. Commun.* 344, 500–510. <https://doi.org/10.1016/j.bbrc.2006.03.163>.
 42. Wang, X., and Schwarz, T.L. (2009). The mechanism of Ca²⁺-dependent regulation of kinesin-mediated mitochondrial motility. *Cellule* 136, 163–174. <https://doi.org/10.1016/j.cell.2008.11.046>.
 43. Saotome, M., Safiulina, D., Szabadkai, G., Das, S., Fransson, A., Aspenstrom, P., Rizzuto, R., and Hajnóczky, G. (2008). Bidirectional Ca²⁺-dependent control of mitochondrial dynamics by the Miro GTPase. *Proc. Natl. Acad. Sci. USA* 105, 20728–20733. <https://doi.org/10.1073/pnas.0808953105>.
 44. Klosowiak, J.L., Focia, P.J., Chakravarthy, S., Landahl, E.C., Freymann, D.M., and Rice, S.E. (2013). Structural coupling of the EF hand and C-terminal GTPase domains in the mitochondrial protein Miro. *EMBO Rep.* 14, 968–974. <https://doi.org/10.1038/embor.2013.151>.
 45. Ling, S., He, Y., Li, X., Hu, M., Ma, Y., Li, Y., Lu, Z., Shen, S., Kong, B., Zou, X., et al. (2020). CircRHOT1 mediated cell proliferation, apoptosis and invasion of pancreatic cancer cells by sponging miR-125a-3p. *J. Cell Mol. Med.* 24, 9881–9889. <https://doi.org/10.1111/jcmm.15572>.
 46. Qu, S., Hao, X., Song, W., Niu, K., Yang, X., Zhang, X., Shang, R., Wang, Q., Li, H., and Liu, Z. (2019). Circular RNA circRHOT1 is upregulated and promotes cell proliferation and invasion in pancreatic cancer. *Epigenomics* 11, 53–63. <https://doi.org/10.2217/epi-2018-0051>.
 47. Ren, X., Yu, J., Guo, L., and Ma, H. (2021). Circular RNA circRHOT1 contributes to pathogenesis of non-small cell lung cancer by epigenetically enhancing C-MYC expression through recruiting KAT5. *Aging (Albany NY)* 13, 20372–20382. <https://doi.org/10.18632/aging.203417>.
 48. Wang, L., Long, H., Zheng, Q., Bo, X., Xiao, X., and Li, B. (2019). Circular RNA circRHOT1 promotes hepatocellular carcinoma progression by initiation of NR2F6 expression. *Mol. Cancer* 18, 119. <https://doi.org/10.1186/s12943-019-1046-7>.
 49. Hussein, N.A., El Sewedy, S.M., Zakareya, M.M., Youssef, E.A., and Ibrahim, F.A.R. (2023). Expression status of circ-SMARCA5, circ-NOL10, circ-LDLRAD3, and circ-RHOT1 in patients with colorectal cancer. *Sci. Rep.* 13, 13308. <https://doi.org/10.1038/s41598-023-40358-4>.
 50. Jiang, W., Yu, Y., Ou, J., Li, Y., and Zhu, N. (2023). Exosomal circRNA RHOT1 promotes breast cancer progression by targeting miR-204-5p/PRMT5 axis. *Cancer Cell Int.* 23, 260. <https://doi.org/10.1186/s12935-023-03111-5>.
 51. Li, Q., Yao, L., Wei, Y., Geng, S., He, C., and Jiang, H. (2015). Role of RHOT1 on migration and proliferation of pancreatic cancer. *Am. J. Cancer Res.* 5, 1460–1470.
 52. Cangkrama, M., Liu, H., Whipman, J., Zubair, M., Matsushita, M., Di Filippo, M., Kopf, M., Innocenti, M., and Werner, S. (2022). A Protumorigenic mDia2-MIRO1 Axis Controls Mitochondrial Positioning and Function in Cancer-Associated Fibroblasts. *Cancer Res.* 82, 3701–3717. <https://doi.org/10.1158/0008-5472.CAN-22-0162>.
 53. Furnish, M., Boulton, D.P., Genter, V., Grofova, D., Ellinwood, M.L., Romero, L., Lucia, M.S., Cramer, S.D., and Caino, M.C. (2022). MIRO2 Regulates Prostate Cancer Cell Growth via GCN1-Dependent Stress Signaling. *Mol. Cancer Res.* 20, 607–621. <https://doi.org/10.1158/1541-7786.MCR-21-0374>.

54. Boulton, D.P., and Caino, M.C. (2024). Emerging roles for Mitochondrial Rho GTPases in tumor biology. *J. Biol. Chem.* *300*, 107670. <https://doi.org/10.1016/j.jbc.2024.107670>.
55. Modi, S., López-Doménech, G., Half, E.F., Covill-Cooke, C., Ivankovic, D., Melandri, D., Arancibia-Cárcamo, I.L., Burden, J.J., Lowe, A.R., and Kittler, J.T. (2019). Miro clusters regulate ER-mitochondria contact sites and link cristae organization to the mitochondrial transport machinery. *Nat. Commun.* *10*, 4399. <https://doi.org/10.1038/s41467-019-12382-4>.
56. Nagy, A. (2000). Cre recombinase: the universal reagent for genome tailoring. *Genesis* *26*, 99–109.
57. Kim, H., Kim, M., Im, S.K., and Fang, S. (2018). Mouse Cre-LoxP system: general principles to determine tissue-specific roles of target genes. *Lab. Anim. Res.* *34*, 147–159. <https://doi.org/10.5625/lar.2018.34.4.147>.
58. Friedrich, G., and Soriano, P. (1991). Promoter traps in embryonic stem cells: a genetic screen to identify and mutate developmental genes in mice. *Genes Dev.* *5*, 1513–1523. <https://doi.org/10.1101/gad.5.9.1513>.
59. Ventura, A., Kirsch, D.G., McLaughlin, M.E., Tuveson, D.A., Grimm, J., Lintault, L., Newman, J., Reczek, E.E., Weissleder, R., and Jacks, T. (2007). Restoration of p53 function leads to tumour regression in vivo. *Nature* *445*, 661–665. <https://doi.org/10.1038/nature05541>.
60. Kanfer, G., Courthéoux, T., Peterka, M., Meier, S., Soste, M., Melnik, A., Reis, K., Aspenström, P., Peter, M., Picotti, P., and Kornmann, B. (2015). Mitotic redistribution of the mitochondrial network by Miro and Cenp-F. *Nat. Commun.* *6*, 8015. <https://doi.org/10.1038/ncomms9015>.
61. Barrasso, A.P., Tong, X., and Poche, R.A. (2018). The mito::mKate2 mouse: A far-red fluorescent reporter mouse line for tracking mitochondrial dynamics in vivo. *Genesis* *56*, e23087. <https://doi.org/10.1002/dvg.23087>.
62. Henrichs, V., Grycova, L., Barinka, C., Nahacka, Z., Neuzil, J., Diez, S., Rohlena, J., Braun, M., and Lansky, Z. (2020). Mitochondria-adapter TRAK1 promotes kinesin-1 driven transport in crowded environments. *Nat. Commun.* *11*, 3123. <https://doi.org/10.1038/s41467-020-16972-5>.
63. Puttrich, V., Rohlena, J., Braun, M., and Lansky, Z. (2022). In Vitro Reconstitution of Molecular Motor-Driven Mitochondrial Transport. *Methods Mol. Biol.* *2431*, 533–546. https://doi.org/10.1007/978-1-0716-1990-2_28.
64. Chevrollier, A., Cassereau, J., Ferré, M., Alban, J., Desquirit-Dumas, V., Gueguen, N., Amati-Bonneau, P., Procaccio, V., Bonneau, D., and Reynier, P. (2012). Standardized mitochondrial analysis gives new insights into mitochondrial dynamics and OPA1 function. *Int. J. Biochem. Cell Biol.* *44*, 980–988. <https://doi.org/10.1016/j.biocel.2012.03.006>.
65. Vander Heiden, M.G., and DeBerardinis, R.J. (2017). Understanding the Intersections between Metabolism and Cancer Biology. *Cell* *168*, 657–669. <https://doi.org/10.1016/j.cell.2016.12.039>.
66. Lin, Y., Yang, B., Huang, Y., Zhang, Y., Jiang, Y., Ma, L., and Shen, Y.Q. (2023). Mitochondrial DNA-targeted therapy: A novel approach to combat cancer. *Cell Insight* *2*, 100113. <https://doi.org/10.1016/j.cellin.2023.100113>.
67. Vodicka, P., Vodenkova, S., Danesova, N., Vodickova, L., Zobalova, R., Tomasova, K., Boukalova, S., Berridge, M.V., and Neuzil, J. (2024). Mitochondrial DNA damage, repair, and replacement in cancer. *Trends Cancer Oct* *21*:S2405-8033(24)00212-7. <https://doi.org/10.1016/j.trecan.2024.09.010>.
68. Dominic, A., Hamilton, D., and Abe, J.I. (2021). Mitochondria and chronic effects of cancer therapeutics: The clinical implications. *J. Thromb. Thrombolysis* *51*, 884–889. <https://doi.org/10.1007/s11239-020-02313-2>.
69. Gorini, S., De Angelis, A., Berrino, L., Malara, N., Rosano, G., and Ferraro, E. (2018). Chemotherapeutic Drugs and Mitochondrial Dysfunction: Focus on Doxorubicin, Trastuzumab, and Sunitinib. *Oxid. Med. Cell. Longev.* *2018*, 7582730. <https://doi.org/10.1155/2018/7582730>.
70. Park, J.S., Sharma, L.K., Li, H., Xiang, R., Holstein, D., Wu, J., Lechleiter, J., Naylor, S.L., Deng, J.J., Lu, J., and Bai, Y. (2009). A heteroplasmic, not homoplasmic, mitochondrial DNA mutation promotes tumorigenesis via alteration in reactive oxygen species generation and apoptosis. *Hum. Mol. Genet.* *18*, 1578–1589. <https://doi.org/10.1093/hmg/ddp069>.
71. Ishikawa, K., Takenaga, K., Akimoto, M., Koshikawa, N., Yamaguchi, A., Imanishi, H., Nakada, K., Honma, Y., and Hayashi, J.I. (2008). ROS-generating mitochondrial DNA mutations can regulate tumor cell metastasis. *Science* *320*, 661–664. <https://doi.org/10.1126/science.1156906>.
72. Kim, M., Mahmood, M., Reznik, E., and Gammage, P.A. (2022). Mitochondrial DNA is a major source of driver mutations in cancer. *Trends Cancer* *8*, 1046–1059. <https://doi.org/10.1016/j.trecan.2022.08.001>.
73. Ahmad, T., Mukherjee, S., Pattnaik, B., Kumar, M., Singh, S., Kumar, M., Rehman, R., Tiwari, B.K., Jha, K.A., Barhanpurkar, A.P., et al. (2014). Miro1 regulates intercellular mitochondrial transport & enhances mesenchymal stem cell rescue efficacy. *EMBO J.* *33*, 994–1010. <https://doi.org/10.1002/embj.201386030>.
74. Babenko, V.A., Silachev, D.N., Popkov, V.A., Zorova, L.D., Pevzner, I.B., Plotnikov, E.Y., Sukhikh, G.T., and Zorov, D.B. (2018). Miro1 Enhances Mitochondria Transfer from Multipotent Mesenchymal Stem Cells (MMSC) to Neural Cells and Improves the Efficacy of Cell Recovery. *Molecules* *23*, 687. <https://doi.org/10.3390/molecules23030687>.
75. Tseng, N., Lambie, S.C., Huynh, C.Q., Sanford, B., Patel, M., Herson, P.S., and Ormond, D.R. (2021). Mitochondrial transfer from mesenchymal stem cells improves neuronal metabolism after oxidant injury in vitro: The role of Miro1. *J. Cerebr. Blood Flow Metabol.* *41*, 761–770. <https://doi.org/10.1177/0271678X20928147>.
76. English, K., Shepherd, A., Uzor, N.E., Trinh, R., Kavelaars, A., and Heijnen, C.J. (2020). Astrocytes rescue neuronal health after cisplatin treatment through mitochondrial transfer. *Acta Neuropathol. Commun.* *8*, 36. <https://doi.org/10.1186/s40478-020-00897-7>.
77. Zhang, Y., Yu, Z., Jiang, D., Liang, X., Liao, S., Zhang, Z., Yue, W., Li, X., Chiu, S.M., Chai, Y.H., et al. (2016). iPSC-MSCs with High Intrinsic MIRO1 and Sensitivity to TNF-alpha Yield Efficacious Mitochondrial Transfer to Rescue Anthracycline-Induced Cardiomyopathy. *Stem Cell Rep.* *7*, 749–763. <https://doi.org/10.1016/j.stemcr.2016.08.009>.
78. Li, B., Zhang, Y., Li, H., Shen, H., Wang, Y., Li, X., Cui, G., and Chen, G. (2021). Miro1 Regulates Neuronal Mitochondrial Transport and Distribution to Alleviate Neuronal Damage in Secondary Brain Injury After Intracerebral Hemorrhage in Rats. *Cell. Mol. Neurobiol.* *41*, 795–812. <https://doi.org/10.1007/s10571-020-00887-2>.
79. Zhao, Y., Song, E., Wang, W., Hsieh, C.H., Wang, X., Feng, W., Wang, X., and Shen, K. (2021). Metaxins are core components of mitochondrial transport adaptor complexes. *Nat. Commun.* *12*, 83. <https://doi.org/10.1038/s41467-020-20346-2>.
80. Peterka, M., and Kornmann, B. (2019). Miro-dependent mitochondrial pool of CENP-F and its farnesylated C-terminal domain are dispensable for normal development in mice. *PLoS Genet.* *15*, e1008050. <https://doi.org/10.1371/journal.pgen.1008050>.
81. Rogers, R.S., and Bhattacharya, J. (2013). When cells become organelle donors. *Physiology* *28*, 414–422. <https://doi.org/10.1152/physiol.00032.2013>.
82. Tiwari, V., Koganti, R., Russell, G., Sharma, A., and Shukla, D. (2021). Role of Tunneling Nanotubes in Viral Infection, Neurodegenerative Disease, and Cancer. *Front. Immunol.* *12*, 680891. <https://doi.org/10.3389/fimmu.2021.680891>.
83. Levoux, J., Prola, A., Lafuste, P., Gervais, M., Chevallier, N., Koumraha, Z., Kefi, K., Braud, L., Schmitt, A., Yacia, A., et al. (2021). Platelets facilitate the wound-healing capability of mesenchymal stem cells by mitochondrial transfer and metabolic reprogramming. *Cell Metabol.* *33*, 688–690. <https://doi.org/10.1016/j.cmet.2021.02.003>.
84. König, T., Nolte, H., Aaltonen, M.J., Tatsuta, T., Krols, M., Stroh, T., Langer, T., and McBride, H.M. (2021). MIROs and DRP1 drive mitochondrial-derived vesicle biogenesis and promote quality control. *Nat. Cell Biol.* *23*, 1271–1286. <https://doi.org/10.1038/s41556-021-00798-4>.

85. Rabas, N., Palmer, S., Mitchell, L., Ismail, S., Gohlke, A., Riley, J.S., Tait, S.W.G., Gammage, P., Soares, L.L., Macpherson, I.R., and Norman, J.C. (2021). PINK1 drives production of mtDNA-containing extracellular vesicles to promote invasiveness. *J. Cell Biol.* 220, e202006049. <https://doi.org/10.1083/jcb.202006049>.
86. Zhang, W., Zhou, H., Li, H., Mou, H., Yinwang, E., Xue, Y., Wang, S., Zhang, Y., Wang, Z., Chen, T., et al. (2023). Cancer cells reprogram to metastatic state through the acquisition of platelet mitochondria. *Cell Rep.* 42, 113464. <https://doi.org/10.1016/j.celrep.2023.113464>.
87. AACR Project GENIE Consortium (2017). AACR Project GENIE: Powering Precision Medicine through an International Consortium. *Cancer Discov.* 7, 818–831. <https://doi.org/10.1158/2159-8290.CD-17-0151>.
88. Hsieh, C.H., Li, L., Vanhauwaert, R., Nguyen, K.T., Davis, M.D., Bu, G., Wszolek, Z.K., and Wang, X. (2019). Miro1 Marks Parkinson's Disease Subset and Miro1 Reducer Rescues Neuron Loss in Parkinson's Models. *Cell Metabol.* 30, 1131–1140.e7. <https://doi.org/10.1016/j.cmet.2019.08.023>.
89. Bharat, V., Durairaj, A.S., Vanhauwaert, R., Li, L., Muir, C.M., Chandra, S., Kwak, C.S., Le Guen, Y., Nandakishore, P., Hsieh, C.H., et al. (2023). A mitochondrial inside-out iron-calcium signal reveals drug targets for Parkinson's disease. *Cell Rep.* 42, 113544. <https://doi.org/10.1016/j.celrep.2023.113544>.
90. Feng, R., Li, S., Lu, C., Andreas, C., Stolz, D.B., Mapara, M.Y., and Lentzsch, S. (2011). Targeting the microtubular network as a new anti-myeloma strategy. *Mol. Cancer Therapeut.* 10, 1886–1896. <https://doi.org/10.1158/1535-7163.MCT-11-0234>.
91. Zhou, Q., Cao, T., Li, F., Zhang, M., Li, X., Zhao, H., and Zhou, Y. (2024). Mitochondria: a new intervention target for tumor invasion and metastasis. *Mol. Med.* 30, 129. <https://doi.org/10.1186/s10020-024-00899-4>.
92. Vasan, K., and Chandel, N.S. (2024). Molecular and cellular mechanisms underlying the failure of mitochondrial metabolism drugs in cancer clinical trials. *J. Clin. Invest.* 134, e176736. <https://doi.org/10.1172/JCI176736>.
93. Durkin, M.E., Qian, X., Popescu, N.C., and Lowy, D.R. (2013). Isolation of Mouse Embryo Fibroblasts. *Bio. Protoc.* 3, e908. <https://doi.org/10.21769/bioprotoc.908>.
94. Yamano, T., Zetsche, B., Ishitani, R., Zhang, F., Nishimasu, H., and Nureki, O. (2017). Structural Basis for the Canonical and Non-canonical PAM Recognition by CRISPR-Cpf1. *Mol. Cell* 67, 633–645.e3. <https://doi.org/10.1016/j.molcel.2017.06.035>.
95. Concordet, J.P., and Haeussler, M. (2018). CRISPOR: intuitive guide selection for CRISPR/Cas9 genome editing experiments and screens. *Nucleic Acids Res.* 46, W242–W245. <https://doi.org/10.1093/nar/gky354>.
96. Hadrava Vanova, K., Pang, Y., Krobava, L., Kraus, M., Nahacka, Z., Boukalova, S., Pack, S.D., Zobalova, R., Zhu, J., Huynh, T.T., et al. (2022). Germline SUCLG2 Variants in Patients With Pheochromocytoma and Paraganglioma. *J. Natl. Cancer Inst.* 114, 130–138. <https://doi.org/10.1093/jnci/djab158>.
97. Nguyen, T.T., Oh, S.S., Weaver, D., Lewandowska, A., Maxfield, D., Schuler, M.H., Smith, N.K., Macfarlane, J., Saunders, G., Palmer, C.A., et al. (2014). Loss of Miro1-directed mitochondrial movement results in a novel murine model for neuron disease. *Proc. Natl. Acad. Sci. USA* 111, E3631–E3640. <https://doi.org/10.1073/pnas.1402449111>.
98. Wittig, I., Braun, H.P., and Schägger, H. (2006). Blue native PAGE. *Nat. Protoc.* 1, 418–428. <https://doi.org/10.1038/nprot.2006.62>.
99. Simoes, R.F., Oliveira, P.J., Cunha-Oliveira, T., and Pereira, F.B. (2022). Evaluation of 6-Hydroxydopamine and Rotenone In Vitro Neurotoxicity on Differentiated SH-SY5Y Cells Using Applied Computational Statistics. *Int. J. Mol. Sci.* 23, 3009. <https://doi.org/10.3390/ijms23063009>.
100. Sousa, B., Pereira, J., Marques, R., Grilo, L.F., Pereira, S.P., Sardão, V.A., Schmitt, F., Oliveira, P.J., and Paredes, J. (2020). P-cadherin induces anoikis-resistance of matrix-detached breast cancer cells by promoting pentose phosphate pathway and decreasing oxidative stress. *Biochim. Biophys. Acta, Mol. Basis Dis.* 1866, 165964. <https://doi.org/10.1016/j.bbadis.2020.165964>.
101. Schindelin, J., Arganda-Carreras, I., Frise, E., Kaynig, V., Longair, M., Pietzsch, T., Preibisch, S., Rueden, C., Saalfeld, S., Schmid, B., et al. (2012). Fiji: an open-source platform for biological-image analysis. *Nat. Methods* 9, 676–682. <https://doi.org/10.1038/nmeth.2019>.
102. Lemaitre, R.P., Bogdanova, A., Borgonovo, B., Woodruff, J.B., and Drechsel, D.N. (2019). FlexiBAC: a versatile, open-source baculovirus vector system for protein expression, secretion, and proteolytic processing. *BMC Biotechnol.* 19, 20. <https://doi.org/10.1186/s12896-019-0512-z>.
103. Aricescu, A.R., Lu, W., and Jones, E.Y. (2006). A time- and cost-efficient system for high-level protein production in mammalian cells. *Acta Crystallogr. D. Biol. Crystallogr.* 62, 1243–1250. <https://doi.org/10.1107/S0907444906029799>.

STAR★METHODS

KEY RESOURCES TABLE

REAGENT or RESOURCE	SOURCE	IDENTIFIER
Antibodies		
Anti- β -Actin (13E5)	Cell Signaling Technology	Cat#4970; RRID: AB_2223172
Anti- β -Actin (8H10D10)	Cell Signaling Technology	Cat#3700; RRID: AB_2242334
Anti- β -Tubulin	Sigma-Aldrich	Cat#T7816; RRID: AB_261770
Anti-ATP5B	Sigma-Aldrich	Cat#HPA001520; RRID: AB_1078243
Anti-DNA	PROGEN Biotechnik	Cat#61014; RRID: AB_2750935
Anti-HSP60	Cell Signaling Technology	Cat#12165; RRID: AB_2636980
Anti-MTCO1 (1D6E1A8)	Abcam	Cat#ab14705; RRID: AB_2084810
Anti-NDUFA9 (20C11B11B11)	Abcam	Cat#ab14713; RRID: AB_301431
Anti-RHOT1 (Miro1)	Atlas Antibodies	Cat#AMAb90852; RRID: AB_2665691
Anti-RHOT2 (Miro2)	NeuroMab	Cat#75-365; RRID: AB_2315894
Anti-SDH5 (SDHAF2)	Cell Signaling Technology	Cat#45849; RRID: AB_2799291
Anti-SDHB (EPR13042(B))	Abcam	Cat#ab178423; RRID: AB_2861366
Anti-SDHB	Abcam	Cat#ab14714; RRID: AB_301432
Abberior STAR RED	Abberior	Cat#STRED-1001-500UG; RRID: AB_3068620
Abberior STAR 580	Abberior	Cat#ST580-1002-500UG; RRID: AB_2910107
Anti-TOMM20 (EPR15581-54)	Abcam	Cat#ab186735; RRID: AB_2889972
Anti-Tom20	Santa Cruz Biotechnology	Cat#sc-11415; RRID: AB_2207533
Anti-UQCRC2	Abcam	Cat#ab14745; RRID: AB_2213640
Bacterial and virus strains		
Endura chemically competent bacteria	VWR	Cat#71003-032
One Shot™ Stbl3™ chemically competent <i>E. coli</i>	Thermo Fisher Scientific	Cat#C737303
Chemicals, peptides, and recombinant proteins		
6-Aminocaproic acid	Sigma-Aldrich	Cat#A2504
4-hydroxytamoxifen	Sigma-Aldrich	Cat#H6278
4-bromoanisole (BAN)	Molecular Center Research	Cat#NC9734505
ADP	Sigma-Aldrich	Cat#A5285
Alexa Fluor™ 488 Phalloidin	Thermo Fisher Scientific	Cat#A12379
Antimycin A	Sigma-Aldrich	Cat#A8674
Benzonase	Merck	Cat#9025-65-4
Carbonyl cyanide 3-chlorophenylhydrazone (CCCP)	Sigma-Aldrich	Cat#C2759
CellMask™ Orange Plasma Membrane Stain	Thermo Fisher Scientific	Cat#C10045
Cytochrome c	Sigma-Aldrich	Cat#C3131
Dichlorodimethylsilane	Sigma-Aldrich	Cat#440272
Digitonin	Sigma-Aldrich	Cat#D141
EMbed-812 kit	EMS	Cat#14120
EMS Grid 200 Mesh, Square, Cu	EMS	Cat#EMS200-Cu
EMS Grid Oval Hole 2 × 1 mm, Cu	EMS	Cat#EMS2010-Cu
FastDigest Bpil	Thermo Fisher Scientific	Cat#FD1014
FreeStyle™ F17 Expression Medium	Gibco	Cat#A1383501

(Continued on next page)

Continued

REAGENT or RESOURCE	SOURCE	IDENTIFIER
Glutamate	Sigma-Aldrich	Cat#G1626
HisPur™ Ni-NTA Superflow Agarose	Thermo Fisher Scientific	Cat#25215
lactobionic acid	Sigma-Aldrich	Cat#153516
Lipofectamine 3000	Thermo Fisher Scientific	Cat#L3000008
Malate	Sigma-Aldrich	Cat#M1000
MesenCult Expansion Kit (Mouse)	Scintila	Cat#05513
MitoTracker™ Deep Red	Thermo Fisher Scientific	Cat#M22426
Oligomycin	Sigma-Aldrich	Cat#4876
Osmium Tetroxide 2% Aqueous Solution	EMS	Cat#19152
Phosphatase Inhibitor Cocktail	Thermo Fisher Scientific	Cat#A32957
Polyethylenimine	Plysciences	Cat#24313-2
Potassium cyanide (KCN)	Sigma-Aldrich	Cat#60178
Potassium ferricyanide	Penta Chemicals	Cat#13850-31000
Protease Inhibitor Cocktail	Sigma-Aldrich	Cat#P2714
Proteinase K from Tritirachium album	Sigma-Aldrich	Cat#P4850
Pyruvate	Sigma-Aldrich	Cat#P5280
RNAzol	Molecular Research Center	Cat#RB192
Rotenone	Sigma-Aldrich	Cat#R8875
Sodium Cacodylate trihydrate	Sigma-Aldrich	Cat#C0250-10G
Strep-Tactin®XT 4Flow® column	IBA	Cat#2-5012-001
Succinate	Sigma-Aldrich	Cat#S9637
Superose 6 10/300 GL column	Merck	Cat#GE29-0915-96
SYBR™ Safe DNA Gel Stain	Thermo Fisher Scientific	Cat#S33102
T4 DNA Ligase	Thermo Fisher Scientific	Cat#15224017
T4 Polynucleotide Kinase	Thermo Fisher Scientific	Cat#EK0031
tamoxifen	Sigma-Aldrich	Cat#T5648
taurine	Sigma-Aldrich	Cat#T0625
Tetramethyl- <i>p</i> -phenylenediamine dihydrochloride (TMPD)	Sigma-Aldrich	Cat#T3134
Tetramethylrhodamine, methyl ester	Sigma-Aldrich	Cat#T5428
Uranyl acetate	EMS	Cat#22400
Uridine	Sigma-Aldrich	Cat#U3750
VECTASHIELD® Antifade Mounting Medium	Vector Laboratories	Cat#H-1000-10
Critical commercial assays		
CellTiter-Glo Luminescent Cell Viability Assay	Promega	Cat#G7570
DirectPCR Lysis Reagent (Mouse Tail)	Viagen	Cat#101-T
DreamTaq Green PCR Master Mix (2X)	Thermo Fisher Scientific	Cat#K1081
DreamTaq PCR Master Mix (2X)	Thermo Fisher Scientific	Cat#K1072
Gel and PCR Clean-up	Macherey-Nagel	Cat#740609
HOT FIREPol EvaGreen qPCR Supermix	Solis Biodyne	Cat#08-36-00020
<i>In Situ</i> Cell Death Detection Kit, Fluorescein	Sigma-Aldrich/Roche	Cat#11684795910
NuceloSpin Plasmid (no lid)	Macherey-Nagel	Cat#740499

(Continued on next page)

Continued

REAGENT or RESOURCE	SOURCE	IDENTIFIER
NucleoBond Xtra Midi	Macherey-Nagel	Cat#740410
PEG-it Virus Precipitation Solution	System Biosciences	Cat#LV810A-1
Pierce BCA Protein Assay Kit	Thermo Fisher Scientific	Cat#23225
Pierce ECL Western Blotting Substrate	Thermo Fisher Scientific	Cat#34095
Radiance ECL	Azure Biosystems	Cat#AC2204
Radiance Plus	Azure Biosystems	Cat#AC2103
RevertAid RT Reverse Transcription Kit	Thermo Fisher Scientific	Cat#K1691
SuperSignal West Femto Maximum Sensitivity Substrate	Thermo Fisher Scientific	Cat#32209
SYLGARD™ 184 Silicone Elastomer Kit	Dow	Cat#1673921
Wizard SV genomic DNA Purification System	Promega	Cat#A2361

Deposited data

Sholl-based analysis script (FIJI)	Mendeley	Mendeley Data: https://doi.org/10.17632/nv8swjd277.1
------------------------------------	----------	--

Experimental models: Cell lines

B16-F1	ATCC	ATCC Cat#CRL-6323; RRID: CVCL_0158
B16 ρ^0	our laboratory ³³	–
B16 ρ^0 GFP	This paper	–
B16 Miro1 ^{KO}	This paper	–
B16 ρ^0 Miro1 ^{KO}	This paper	–
B16 ρ^0 GFP D5-D20	This paper	Tumor-derived cell lines D5, D10, D15 and D20. Isolated from C57BL/6 ^{Gt(Rosa)26Sor(CAG-Flo,-EYFP)x Rhot1tm1a} and C57BL/6 ^{Rhot1 Tm1c Rosa-creERT2} mice
MEF	This paper	Isolated from C57BL/6 ^{Rhot1 Tm1c Rosa-creERT2} mice
MSC	This paper	Isolated from C57BL/6, C57BL/6 ^{Tg(CAG-mKate2)} , C57BL/6 ^{Gt(Rosa)26Sor(CAG-Flo,-EYFP)} , C57BL/6 ^{Rhot1 Tm1c Rosa-creERT2} or C57BL/6 ^{Gt(Rosa)26Sor(CAG-Flo,-EYFP)x Tg(CAG-mKate2)1Poche/JC57BL/6J} , C57BL/6 ^{Rhot1 Tm1c Rosa-creERT2x Tg(CAG-mKate2)1Poche/JC57BL/6J} mice
HCmel12	gifted by A. Viros (Cancer Research UK Manchester Institute)	–
HCmel12 ρ^0	gifted by P.A. Gammage (Cruk Institute, Glasgow UK)	–
HEK293T	gifted by A. Aricescu ¹⁰³ (University of Oxford, England)	–
Sf9-ESF	Expression systems	Cat#94-001F

Experimental models: Organisms/strains

Mouse: C57BL/6J	Jackson Laboratory	Stock No. 000664
Mouse: C57BL/6 Tg(CAG-mKate2)	Jackson Laboratory	Stock No. 032188 ⁶¹
Mouse: C57BL/6 Gt(Rosa)26Sor (CAG-Flo,-EYFP) x Rhot1tm1a	our laboratory, RHOT1 allele purchased from Jackson Laboratory	Stock No. 031126 ⁹⁷
Mouse: C57BL/6 Rhot1 Tm1c Rosa-creERT2	our laboratory, R26-CreERT2 allele purchased from Jackson Laboratory	Stock No. 008463 ⁵⁹
Mouse: C57BL/6 Gt(Rosa)26Sor (CAG-Flo,-EYFP) x Rhot1tm1a x Tg (CAG-mKate2)1Poche/JC57BL/6J	our laboratory	–

(Continued on next page)

Continued		
REAGENT or RESOURCE	SOURCE	IDENTIFIER
Mouse: C57BL/6 Rhot1 Tm1c Rosa-creERT2 x Tg(CAG-mKate2) 1Poche/JC57BL/6J	our laboratory	–
Oligonucleotides		
See Table S1 for sequences of oligonucleotides	–	–
Recombinant DNA		
KIF5B cDNA	Dharmacon Reagents	GenBank: BC126281.1
mCherry-TRAK1 (KIAA1042)	Kazusa DNA Research Institute	UniProtKB: Q9UPV9
Plasmid pKAM-GFP	Addgene	Addgene #101865; unpublished
pX AsCpf1-Venus-NLS	gifted by Björn Schuster, (Institute of Molecular Genetics, CAS, CR; PI Petr Bartunek)	–
psPAX2	Addgene	Addgene #12260; unpublished
pMD2.G	Addgene	Addgene #12259; unpublished
Software and algorithms		
Adobe Photoshop CS6	http://www.adobe.com/uk/products/photoshop.html	N/A
Adobe Illustrator CS6	https://www.adobe.com/products/illustrator.html	N/A
CorelDRAW Graphics Suite 2019	https://www.coreldraw.com	N/A
Graphpad Prism 8	http://graphpad.com/scientific-software/prism/	N/A
SeqMan Pro	https://www.dnastar.com/software/	N/A
Crispor	http://crispor.org	Concordet and Haeussler ⁹⁵
NIS-elements	https://www.microscope.healthcare.nikon.com/en_EU/products/software/nis-elements	N/A
Amira	https://www.thermofisher.com/cz/en/home/electron-microscopy/products/software-em-3d-vis/amira-software.html	N/A
FIJI	http://Fiji.sc/	Schindelin et al. ¹⁰¹
Leica Application Suite X	https://www.leica-microsystems.com/products/microscope-software/p/leica-las-x-ls/	N/A
Version Wave Desktop 2.6	Agilent	N/A
XF Report Generators	Agilent	N/A
FlowJo v10 software	www.flowjo.com	N/A
Imaris 9.9.1	https://imaris.oxinst.com/	N/A
TSE PhenoMaster v.7.1.2	https://www.tse-systems.com/	N/A
Other		
Cytochips	CYTOO SA	Cat#Y-S-FN X18, Cat#Y-M-FN X18
NativePAGE 4 to 16%, Bis-Tris, 1.0 mm, Mini Protein Gels	Thermo Fisher Scientific	Cat#BN1002BOX

(Continued on next page)

Continued

REAGENT or RESOURCE	SOURCE	IDENTIFIER
NativePAGE 3 to 12%, Bis-Tris, 1.0 mm, Mini Protein Gels	Thermo Fisher Scientific	Cat#BN1001BOX
Litographic mask	Compugraphics	N/A
3-inch silicone wafers	MicroChemicals	N/A
SU-8 3000 Permanent Negative Epoxy Photoresist	Kayaku Advanced Materials	N/A

EXPERIMENTAL MODEL AND STUDY PARTICIPANT DETAILS

Cell culture

The cell lines have not been authenticated. All cell lines were regularly tested for mycoplasma contamination by MycoAlert Detection kit (Lonza Bioscience). B16 mouse metastatic melanoma cells were purchased from the ATCC and cultured in DMEM supplemented with 10% FBS and antibiotics at 37°C and 5% CO₂. Cells devoid of mtDNA, B16 ρ^0 , were cultivated in the presence of 1 mM pyruvate and 50 mg/mL uridine. B16 ρ^0 were generated through long-term treatment with ethidium bromide, as previously described.³³

Tumor-derived D5, D10, D15 and D20 sublines were prepared following injection of B16 ρ^0 cells with cytoplasmic expression of green fluorescent protein (B16 ρ^0 GFP cells) subcutaneously (s.c.) into C57BL/6 mito::mKate2 Ctrl and C57BL/6 mito::mKate2 Miro1^{KO} mice at 10⁶ cells per animal. The animals were sacrificed on day 5, 10, 15 and 20 (D5, D10, D15 and D20 respectively), the pre-tumor lesions or tumors excised, and cells isolated from the tissue as described.³³ To obtain a sufficient number of tumor cells to derive the cell lines to culture, we combined tumor plaques from several mice into a single culture (2–3 mice per cell line). The tumor plaques of B16 ρ^0 GFP cells were dissected, cut into small pieces, and cultured to allow the cells to migrate out of the tumor. The cells were then cultured for several weeks (4–6 weeks for each) in media supplemented with 1 mM pyruvate and 50 mg/mL uridine to support their replication even in the absence of mtDNA and to obtain an efficient number of cells, after which they were aliquoted and frozen. Given the Hayflick limit of non-tumor stromal cells and the rapid proliferation rate of B16 cells (approximately 1.5 divisions per 24 h), the tumor cells outgrew the non-tumor cells during the culture period. As a result, no additional selection was necessary. The cell lines were then utilized in the standard manner typical for established cell lines, undergoing multiple freeze-thaw cycles and being used for several weeks in each experiment over a span of several years. All tumor-derived cell lines were kept in DMEM media containing 1 mM pyruvate and 50 mg/mL uridine.

HCmel12 were gifted by A. Viros (Cancer Research UK Manchester Institute) and cultured in DMEM supplemented with 10% FBS, 2mM glutamine and antibiotics at 37°C and 5% CO₂. HCmel12 ρ^0 , were additionally cultivated in the presence of 20% FBS, 1 mM pyruvate and 50 mg/mL uridine. HCmel12 ρ^0 were prepared as following. Wildtype HCmel12 melanoma cells were treated with 500 ng/mL ethidium bromide (EtBr) in the culture medium for 10 days to deplete them of mtDNA. The surviving cells were clone-diluted in 96-well plates (seeding 0.8 cells per well) with conditioned medium. Each clone was then isolated, expanded, and evaluated for presence of mtDNA by competitive PCR. Clones exhibiting a band for mtDNA were discarded, with the ones remaining being further assessed to confirm depletion of mtDNA by ddPCR. Only clones in which mtDNA was absent were kept and designated as rho0 (ρ^0).

MEF cells were prepared following the procedure outlined by Durkin et al. in 2013.⁹³ To generate these cells, 13.5-day-old embryos from C57BL/6 Rhot1 Tm1c Rosa-creERT2 mice were utilized. After euthanization of pregnant female, embryos were carefully extracted from the uterine cavity, with the head and red tissues (such as heart and liver) subsequently removed. The embryonic bodies were then finely chopped and minced in 0.25% trypsin-EDTA (T/E) solution. Following this, the suspension of embryo pieces was thoroughly disaggregated through repeated pipetting in DMEM medium. The supernatant containing the MEF cells was transferred to a flask filled with fresh DMEM medium containing 10% FBS and antibiotics, and the cells were subsequently cultured under standard conditions. For the induction of Miro1^{KO} *in vitro*, MEF cells isolated from C57BL/6 Rhot1 Tm1c Rosa-creERT2 mice were treated (controls were non-treated) with 15 μ M 4-hydroxytamoxifen (Sigma-Aldrich) for a period of 5 days.

MSCs were isolated from bone marrow of C57BL/6 mito::mKate2, C57BL/6Gt(Rosa)26Sor(CAG-Fipo,-EYFP) x Rhot1tm1a) and C57BL/6 Rhot1 Tm1c Rosa-creERT2with or without mito::mKate2 fluorescence, with the use of MesenCult Expansion Kit(Scintilla) according to the manufacturer's protocol. The isolation was done either from uninduced C57BL/6 Rhot1 Tm1c Rosa-creERT2 and Miro1 knockout was induced *in vitro*(Ctrl samples as uninduced) as described further or directly from Ctrl and Miro1^{KO} micewhere both types of mice had been treated with tamoxifen via intraperitoneal injections (administered over five consecutive days, followed by a three-week interval, the period needed to ensure full knockout), prior to MSC isolation.

Briefly, the femurs and tibias were removed from sacrificed mice, and bone marrow was flushed, resuspended in MesenCult expansion media with MesenPure and seeded in culture flasks. Cells were further cultured for up to 10 passages. MSCs were used for experiments between passages 3 and 10. For the induction of Miro1^{KO} *in vitro*, MSCs isolated from C57BL/6 Rhot1

Tm1c Rosa-creERT2 mice with or without mito::mKate2, were treated for a period of 5 days with 15 μ M 4-hydroxytamoxifen (Sigma-Aldrich).

B16 ρ^0 GFP cells with stable cytoplasmic GFP expression were generated through lentivirus transduction with lentiviral particles carrying the GFP plasmid. Recombinant lentiviruses were produced by calcium-phosphate transfection of HEK 293T cells. The cells were seeded in a 100 mm Petri dish at 30% confluency one day prior to transfection. For transfection, two packaging plasmids, psPAX2 and pMD2.G (Addgene #12260 and #12259, respectively, both gifts from Didier Trono), were used along with the pKAM-GFP plasmid (Addgene #101865, a gift from Archibald Perkins). The packaging plasmids and the GFP plasmid were mixed in a 1:1 ratio (10 μ g each) in 500 μ L of CaCl₂ (final concentration 0.25 mM, Sigma), then 500 μ L of 2xBBA solution (50 mM BES, 280 nM NaCl, 1.5 mM Na₂HPO₄, pH adjusted to 6.9–7; all from Sigma) was added in a dropwise manner. After a 15-min incubation, the solution was added to the cells in a Petri dish containing complete DMEM medium with chloroquine (final concentration 25 μ M, Sigma). The medium containing lentiviral particles was harvested 48 h post-transfection, and the viral particles were precipitated using the virus precipitation solution PEG-it according to the manufacturer's instruction (System Biosciences). Target cells were transduced with viruses at multiplicity of infection MOI 5–10. Cells were then sorted for GFP positivity and used in further experiments.

Miro1^{KO} cell lines were generated by genomic deletion of *RHOT1* gene (Miro1) in B16 and B16 ρ^0 cells was performed using a CRISPR-Cpf1/Cas12 system.⁹⁴ crRNAs were identified using the Ensemble database (<https://www.ensembl.org/index.html>) and the Crispor software (<http://crispor.org>)⁹⁵ targeting exon 3. DNA oligonucleotides were designed as 3 crRNAs (5' → 3' TCT ATA CCA GGC CCT TCT GTT TA, AGG GGT GAC GTC AGC TGG AAT GG, AAG TTA ATG TAA TAG CCC TGA AA) interspaced by PAM sequence AAT TTC TAC TCT TGT AGA T. They were annealed (37°C/30 min, 95°C/5 min, 25°C ramp down 5%/min) and then cloned to the pX AsCpf1/Cas12-Venus-NLS crRNA plasmid (gift from Björn Schuster)⁹⁶ digested with FastDigest Bpil enzyme. Unless stated otherwise, all enzymes were purchased from Thermo Fisher Scientific. Ligation was performed with T4 DNA ligase. Digestion and ligation reaction proceeded according to the manufacturer's instructions. DNA constructs were then transformed into chemically competent bacterial strain Endura (VWR).

Transformation of bacteria proceeded by combining 100 μ L of bacterial aliquot with 5 μ L of the ligation reaction mixture, after which were bacteria incubated for 30 min on ice, exposed to heat-shock for 1 min at 42°C, and placed on ice for 2 min. Bacteria were then transferred to the LB media and cultivated at 37°C on a shaker (200 rpm) for 1 h. Transformed bacteria were plated on agarose plates with ampicillin (Serva). Positive colonies were confirmed by colony PCR using DreamTaq Green PCR Master Mix (2X) and primers specific for the sequence of the Cpf1 vector (forward pXPR: GGA CTA TCA TAT GCT TAC CGT AAC TTG AAA G, reverse sgRNA ivt R: AAA AGC ACC GAC TCG GTG CC). The PCR reaction was conducted according to manufacturer's protocol and products of endpoint PCR were verified by DNA electrophoresis on an agarose gel (2% agarose, 60 V/90 min).

Positive clones were used for inoculating 100 mL of LB media and cultivated overnight at 200 rpm/37°C. Plasmid DNA was isolated using the NucleoBond Xtra Midi kit (Macherey-Nagel) according to manufacturer's instructions. The Cpf1 vector with crRNA targeted to exon 3 of *RHOT1* gene was verified by Sanger sequencing (Eurofins Genomics, forward pXPR: GGA CTA TCA TAT GCT TAC CGT AAC TTG AAA G or reverse sgRNA ivt R: AAA AGC ACC GAC TCG GTG CC). This vector was then used for lipofectamine transfection of B16 and B16 ρ^0 cells.

Transfection of B16 and B16 ρ^0 cells was performed using Lipofectamine 3000 (Thermo Fisher Scientific) according to manufacturer's protocol, with 2 μ g of plasmid DNA for the transfection reaction. After 48 h, single cell sorting was conducted using BD FACSAria cell sorter where cells were selected for YFP (Venus) positivity. The sorted clones were analyzed using PCR and DNA electrophoresis. To verify the knockout status of the *RHOT1* gene on the level of genomic DNA, we used one forward primer: GTA CAG TAC ACA TTT GGA GGC AAG A and two reverse primers targeting the exon 3 sequence behind PAM3 sequence (reverse 1: TCT CCT CAG CTC TCA AAC TGA CC) or between the PAM2 and PAM3 sequence (reverse 2: TTC ACC CAT CAA AGG CCA CCC). DNA electrophoresis was performed as mentioned above. Positive clones were confirmed by western blotting and Sanger sequencing. For sequencing, cells were seeded on 6 well-plates and DNA was isolated using Wizard SV genomic DNA Purification System (Promega), followed by polymerization by means of the DreamTaq PCR Master Mix (2X) and purification from the agarose gel using a Gel and PCR Clean-up kit (Macherey Nagel). PCR and sequencing reactions were performed the same way as mentioned above using the forward (GTA CAG TAC ACA TTT GGA GGC AAG A) or reverse 1 primer (TCT CCT CAG CTC TCA AAC TGA CC).

Animal models

All animals were crossbred on a C57BL/6J or C57BL/6N background, as further specified. Control Gt(Rosa)26Sor(CAG-Flpo,-EYFP) x Rhot1tm1a mice were generated on C57BL/6N background. For generation of Rhot1tm1c Rosa-CreERT2 mice were C57BL/6N mice containing the DNA cassette with the *RHOT1* gene (Miro1 protein) and exon 2 flanked by two *loxP* sites crossbred with C57BL/6J mice containing tamoxifen inducible (estrogen receptor T2) Rosa-CreERT2 and whole-body expression Rosa26 locus of Cre recombinase. *Rhot1* and *R26-CreERT2* allele were purchased from Jackson Laboratory.^{59,97} Homozygous expression of the *RHOT1* gene and Rosa-CreERT2 was proven by genotyping of mice using DNA isolated from mouse tails as mentioned below. The Tg(CAG-mKate2) mouse strain was obtained from Jackson Laboratory, developed as described⁶¹ and crossbred on C57BL/6J background. Positive animals were selected according to positivity for mKate2. To obtain mice expressing the mito::mKate2 fluorescent protein, we crossbred Gt(Rosa)26Sor(CAG-Flpo,-EYFP) x Rhot1tm1a and Rhot1tm1c Rosa-CreERT2 mice with C57BL/6J x Tg(CAG-mKate2) mice with heterozygous expression of mito::mKate2 targeted to mitochondria. For the induction of Miro1^{KO} for each experiment were Gt(Rosa)

26Sor(CAG-Flpo,-EYFP) x Rhot1tm1a) and Rhot1tm1c Rosa-CreERT2 mice injected with tamoxifen daily for 5 consecutive days (2 mg/20 g mouse in 2% EtOH and corn oil). Three weeks after the final tamoxifen injection (the time required for knockout to take effect), the mice were used for further experiments. Deletion of Miro1 was proven in different tissues by the level of DNA and protein. Miro1^{KO} mice were evaluated for basic hematology, biochemistry, and indirect calorimetry tests (see [Item S1–S3](#)) as specified further.

Preparation of reporter mouse was conducted as follows. We conducted crossbreeding between the Rhot1 Rosa-CreERT2 mouse and a reporter transgenic mouse expressing dTomato/EGFP fluorescence on C57BL/6J background, with expression patterns dependent on the knockout status (dTomato indicating no recombination and EGFP indicating recombination). The offspring generation was then injected intraperitoneally with tamoxifen as described above. Ctrl (uninduced) and Miro1^{KO} mice were further used for experiments (see *In Vivo* Experiments).

We have used male and female mice randomly distributed in experimental groups, both 6–12 weeks of age at the beginning of the experiment. The sex of the mice did not influence the study data. All animal care and experimental protocols were designed and conducted in accordance with the guidelines of the Animal Care Committee of Czech Academy of Sciences and by Ministry of Health of the Czech Republic and in agreement with the Animal Protection Law of the Czech Republic (licence number AV CR 9082/2021 SOVII, AV CR 6219/2021 SOVII, 73/2019 and PP465/2017_HFD). Mice were housed under standard conditions with a 12h light/dark cycle and given *ad libitum* access to food and water.

Hematology analysis

For hematology parameters assessment (see [Item S1](#)), approximately 0.1 mL of blood per animal was collected by orbital plexus bleeding to the 1 mL microtubes containing EDTA. The microtubes with the blood were immediately tested after dilution of the blood 10x with dilution buffer using BC-5300Vet Auto Hematology Analyzer with validated methods for assessment of hematology parameters (Complete Blood Count with Differentials).

Biochemistry analysis

For biochemical parameters assessment (see [Item S2](#)), approximately 1 mL of blood per animal was collected by orbital plexus bleeding to the 1 mL microtubes containing Li-heparin. The microtubes with the blood were kept at least 30 min in ice until the plasma was isolated by centrifugation technique (10 min, 5000 rpm, at 4°C). The isolated plasma was tested using automatic Beckman Coulter AU480 Chemistry Analyzer, previously calibrated to the tested parameters, using validated methods for assessment of following parameters: Albumin, Total Protein, Total Bilirubin, Alkaline phosphatase (ALP), Aspartate aminotransferase (AST), Alanine aminotransferase (ALT), Urea, Creatinine, Uric Acid, alpha-Amylase, Fructosamine, Glucose, Lipase, Triglycerides, Cholesterol (total), HDL Cholesterol, Sodium, Potassium, Chloride, Calcium and inorganic Phosphorus. The program compared the measured values with the acceptable range of the standard and quality control, and also monitored compliance with the set quality control rule.

Indirect calorimetry

Indirect calorimetry was performed by PhenoMaster (TSE Systems, Bad Homburg, Germany, TSE PhenoMaster v.7.1.2 software). The mice were weighted before introducing into the cage of the calorimetric system and measured individually. Mice were provided *ad libitum* access to water and food, standard chow diet (Altromin 1314, Lage, Germany) or High fat diet (HFD) (Ssniff D12492(l) mod., Soest, Germany), depending on the experimental group.

For HFD experiments (see [Item S3](#)), 14 male mice based on C57Bl/6 background were used, Rhot1 Tm1c Rosa-creERT2 x Rhot1 Tm1c Rosa-creERT2 positive for Cre, $n = 7$ and Gt(Rosa)26Sor(CAG-Flpo,-EYFP) x Rhot1tm1a mice negative for Cre considered as control group, $n = 7$, were induced with tamoxifen as described previously at the age of 7 weeks, and administrated with High fat diet (HFD) (Ssniff D12492(l) mod., Soest, Germany) at 16 weeks old for 15 weeks. The body weight was monitored weekly until the mice were 31 week old.

METHOD DETAILS

Genotyping of mice

Isolation of genomic DNA from mouse tails for the purpose of genotyping of the mouse strains was done in 50 mL of Direct PCR lysis Reagent (Viagen) together with Proteinase K (Sigma-Aldrich). Mouse tails were incubated overnight at 55°C. Isolation of DNA from cells and different organs was performed using the Wizard Genomic DNA Purification Kit following manufacturer's protocol (Promega). PCR reaction for both DNA isolated mouse tails and mouse organs, was performed using DreamTaq Green PCR Master Mix (2X) (Thermo Fisher Scientific) and primers for *RHOT1* and *Rosa-CreERT2* detection designed by Jackson Laboratories and purchased from Sigma-Aldrich (See [key resources table](#)). PCR products were analyzed by gel electrophoresis on a 2% agarose gel stained with SYBR safe DNA gel stain (Thermo Fisher Scientific). Electrophoresis was run at constant voltage of 80 V for 1 h and the gel was visualized under ultraviolet (UV) light.

Western blotting

Cells were lysed and organs were homogenized and lysed in RIPA buffer (10 mM Tris, pH 7.4, 1 mM EDTA, 150 mM NaCl, 1% Triton X-100) supplemented with the protease (1:100) and phosphatase (1:10) inhibitor cocktail (Thermo Fisher Scientific). The

lysate was clarified by centrifugation, and protein concentration was determined by BCA assay (Thermo Fisher Scientific). 30–50 μg of protein of each sample was loaded onto a sodium dodecyl sulfate-polyacrylamide gel (SDS-PAGE), separated by electrophoresis at first at 90V for 30 min, then at 120 V for 60–90 min, and transferred to nitrocellulose membranes (Biorad) at 100 V for 90–120 min. The membranes were then blocked using skim milk (Serva) and probed with respective antibodies and β -actin as a loading control. Images were acquired using the Azure c600 imaging system by means of Radiance Ecl or Radiance Plus (Azure Biosystems).

Native blue gel electrophoresis (NBGE)

NBGE was performed as previously published.⁹⁸ In brief, mitochondria were isolated using a Balch-style homogenizer as described in [method details](#) (see “isolation of mitochondria”). 10 μg (for CII, CIII and Hsp60) or 20 μg (for CI and CV) of digitonin-solubilized mitochondria (8 g/g of protein) were mixed with sample loading buffer (0.015 $\mu\text{L}/\mu\text{g}$ protein; 0.75 M 6-aminocaproic acid, 50 mM Bis-Tris, 12% glycerol, 0.5 mM EDTA, 5% Coomassie Brilliant Blue G-250) and separated on NativePAGE Novex BisTris 3%–12% (for CI and CV) or 4–16% (for CII, CIII and Hsp60) gradient gels (Invitrogen). The electrophoresis ran in three steps, i.e., using the blue cathode buffer (15 mM Bis-Tris, 50 mM Tricine, pH 7, 0.02% Coomassie Brilliant Blue G-250) at 35 V for 70 min, and then clear cathode buffer (15 mM Bis-Tris, 50 mM Tricine, pH 7) at 25 V overnight. Finally, the voltage was increased to 200 V for 2 h. After electrophoresis, the gels were incubated in transfer buffer (2.5 mM Tris, 2.5 mM Glycine, 10% methanol) containing 0.1% SDS for 10 min and proteins were transferred to 0.2 μm PVDF (polyvinylidene difluoride) membranes (BioRad) probed with specific antibodies against CI (NDUFA9, Abcam), CII (SDHAF2, Cell Signaling and SDHB, Abcam), CIII (UQCRC2, Abcam), CV (ATP5B, Sigma-Aldrich) and HSP60 (Cell Signaling) as the loading control.

Crystal violet assay

Cells were seeded in 12-well plates at 10,000 per well. After each time point, cells were fixed with 4% paraformaldehyde and stained with crystal violet (0.05% in water) for 1 h. After 3 washing cycles with PBS, crystal violet dye was extracted using 1% SDS, and the absorbance was measured at 595 nm using a microplate reader (Infinite M200, Tecan).

High resolution respirometry

Respiration of cells from cellular culture and homogenized tissues was assessed using the high-resolution Oxygraph-2k respirometer (Oroboros Instruments, Innsbruck, Austria). Briefly, cells were trypsinized, washed with PBS, and resuspended in the Mir05 medium (0.5 mM EGTA, 3 mM MgCl_2 , 60 mM K-lactobionate, 20 mM taurine, 10 mM KH_2PO_4 , 110 mM sucrose, 1 g/L bovine serum albumin, 20 mM HEPES, pH 7.1, 30°C; all purchased from Sigma) at 10^6 per mL. Several milligrams of tissue (approx. 10–20 mg per chamber for liver, approx. 20–50 mg per chamber for lungs) were homogenized using Shredder homogenization (Oroboros) and resuspended in Mir05 medium. The suspension of cells was added to the respirometer chambers and subjected for either non-permeabilized protocol to detect routine respiration (cells from cellular culture only) or permeabilized protocol to detect oxygen consumption via Complex I-IV. For the non-permeabilized protocol, routine respiration was evaluated after addition of 10 mM succinate and 3 mM ADP, then maximal respiration capacity was determined by stepwise addition of carbonyl cyanide 3-chlorophenylhydrazone (CCCP) in presence of 5 nM inhibitor of Complex V (CV) oligomycin. At the end of each experiment, 0.5 μM rotenone (CI inhibitor) and 2.5 μM antimycin A (Complex III (CIII) inhibitor) were added to inhibit the electron transport chain, and the residual oxygen consumption was subtracted from the results to obtain mitochondria-specific values.

For the permeabilized protocol, basal respiration was assessed at 37°C and cells were then permeabilized with digitonin (5 μg per 10^6 cells), followed by sequential additions of substrate and inhibitors. In the case of homogenized tissues, no digitonin is added and the protocol continues directly with the further procedure as following. Complex I (CI) respiration was determined after adding 15 mM glutamate, 3 mM malate, 3 mM ADP, and 10 μM cytochrome c. Complex II (CII) respiration was assessed in the presence of 0.5 μM rotenone (CI inhibitor), 10 mM succinate, 3 mM ADP, and 10 μM cytochrome c. CI + CII respiration was evaluated upon adding glutamate, malate, ADP, cytochrome c, succinate, and rotenone. Maximal respiration capacity was determined by stepwise addition of carbonyl cyanide 3-chlorophenylhydrazone (CCCP). At the end of each experiment, 2.5 μM antimycin A (Complex III (CIII) inhibitor) was added to inhibit the electron transport chain, and the residual oxygen consumption was subtracted from the results in order to obtain mitochondria-specific values. For assessing complex IV (CIV) respiration, 0.5 mM ascorbate and 2 mM tetramethyl-*p*-phenylenediamine dihydrochloride (TMPD) were added after inhibiting CIII, followed by the addition of 2.5 mM potassium cyanide (KCN; CIV inhibitor).

Seahorse measurements

Oxygen consumption rate (OCR) was measured using Seahorse XFe96 Extracellular Flux Analyzer (Agilent Scientific Instruments, Santa Clara, CA, USA) by performing the Mito Stress protocol, as described previously.^{99,100} The cell lines were seeded in Seahorse XF96 cell culture microplates, at a final density of 1×10^4 cells/well, 24 h before the experiment. XFe96 sensor cartridges were placed in a 96-well calibration plate containing 200 μL /well calibration buffer and left to hydrate overnight at 37°C. On the day of the experiment, cells were washed three times with pre-warmed serum-free minimal DMEM medium (D5030, Sigma-Aldrich) supplemented with 25 mM glucose, 4 mM L-glutamine, 1 mM sodium pyruvate, and 5 mM HEPES (pH adjusted to 7.4 with NaOH). Cells were subsequently incubated at 37°C for 1 h in a CO_2 -free atmosphere. OCR measurements were obtained in different respiratory states by sequential injection of 1 μM

oligomycin (port A), 2 μ M FCCP (port B), and 1 μ M rotenone/antimycin (port C) of the XFe96 sensor cartridge. Stock solutions of these reagents were prepared previously in DMSO, and diluted in serum-free DMEM medium, and 25 μ L were added to the respective port of the XFe96 sensor cartridge. After the loading of the compounds, the sensor cartridge and calibration plate were inserted into the XFe96 Extracellular Flux Analyzer for calibration. The calibration plate was then replaced with the experimental plate when the calibration was complete. Three baseline rate measurements of OCR were acquired using a 3-min mix and 5-min measuring cycles. Then, the compounds were automatically and sequentially injected into each well by the XFe96 Analyzer, and OCR was measured using the same cycle parameters as previously described. At the end of the experiment, Hoechst 33342 (1 μ g/mL) was added to each well and used as a fluorescence-based direct cell counting method for normalization purposes by counting nuclei using BioTek Cytation 5 Cell Imaging Multimode Reader (Agilent Scientific Instruments, Santa Clara, CA, USA). The results were analyzed using the Software Version Wave Desktop 2.6 and exported using the respective XF Report Generators (Agilent).

ATP concentration evaluation

Cell lines were seeded in 96-well plates at a final density of 1×10^4 cells/well, 24 h before the experiment. Two hours before the measurement, cells were incubated with either standard media or media containing 25mM 2-deoxy-D-glucose (2-DG, stock solution prepared in media) to inhibit glycolysis. ATP levels were quantified using the Cell-Titer Glo luminescence kit (Promega). Prior to the addition of the CellTiter-Glo reagent, the plate was equilibrated at room temperature for 30 min. Following equilibration, 100 μ L of reagent was added to each well (at a ratio of 1:1 with the culture media), and the plate was placed in an orbital shaker for 2 min, protected from light. The plate was then incubated at room temperature for 10 min to allow the luminescent signal to stabilize. Luminescence was then measured using a microplate reader (Infinite M200, Tecan). The data were normalized to cell mass, which was determined by crystal violet staining in a parallel plate.

Detection of mitochondrial mass by fluorescent cytometry

Cells were harvested by trypsinization, and 10^6 cells stained in 10 mL of complete DMEM with 100 nM MitoTracker Green for 30 min in 37°C in dark. Cells were then spun down 300g/5 min and washed with PBS. Pellets were resuspended in FACS buffer (PBS with 2% FBS), and Hoechst 33258 (10 μ g/mL) was added shortly before measurement.

Tissues from Ctrl, Miro1^{KO} and mKate2 mice were dissected and homogenized using a suspension of Collagenase I (1 mg/mL, skin) or Collagenase IV (1 mg/mL, lung) along with DNase (10 μ g/mL) for 3 h. For tissue samples, an equivalent of 5×10^5 cells was stained in 5 mL of complete medium the same way as described above.

Mitochondrial membrane potential evaluation

Mitochondrial membrane potential ($\Delta\Psi$) was measured in both cell cultures and homogenized tissue samples. For cell culture experiments, cells were seeded at a density of 1×10^5 cells per well in a 12-well plate one day before the measurements were taken. To stain the cells, 50 nM TMRM (Tetramethylrhodamine, Methyl Ester) was added to each well, and the cells were incubated 30 min prior to measurement. Positive control cells were pre-treated with 50 μ M CCCP (Carbonyl cyanide *m*-chlorophenyl hydrazone) for 5–10 min, after which TMRM was added. Cells were then washed with PBS and trypsinized. Cellular pellet was resuspended in 100 μ L of FACS buffer (PBS with 2% FBS) with Hoechst 33258 (10 μ g/mL) used for determining viability.

Tissues from Ctrl and Miro1^{KO} mice were dissected and homogenized using a suspension of Collagenase I (1 mg/mL, skin) or Collagenase IV (1 mg/mL, lung) along with DNase (10 μ g/mL) for 3 h. For tissue samples, an equivalent of 5×10^5 cells was stained in 5 mL of complete medium with 50 nM TMRM for 30 min. Positive control samples were pre-treated with 50 μ M CCCP for 5–10 min before staining. Following staining, all samples were centrifuged and resuspended in 200 μ L of FACS buffer, consisting of PBS with 2% FBS. The samples were then analyzed using flow cytometry (BD Fortessa) to detect mitochondrial potential, with Hoechst 33258 (10 μ g/mL) used for determining viability.

qPCR

Cells were seeded 100 mm Petri dish at a density of 1×10^6 cells 24 h before the RNA isolation. Total RNA was isolated in triplicate from B16, B16 p^0 and B16 p^0 tumor-derived cell lines (D10, D15 and D20) using RNAzol extraction (Molecular Research Center). Cells were lysed with RNAzol, DNA and proteins were precipitated by the addition of water and removed by centrifugation (14,500 g; 15 min; RT). 4-bromoanisole (Molecular Research Center) was added to the supernatants for additional purification, and samples were centrifuged again (14,500 g; 10 min; RT). RNA was precipitated by 1 h incubation of the supernatant with ice-cold isopropanol, pelleted by centrifugation (14,500 g; 15 min; 4°C) and washed with ethanol. The dried RNA was resuspended in RNase-free water, and its purity and concentration were measured by NanoDrop (Thermo Fisher Scientific). 1 μ g of RNA was transcribed to cDNA using RevertAid RT Reverse Transcription Kit (Thermo Fisher Scientific) with random hexamer primer. To assess the expression of target genes (for primer sequences, see [key resources table](#)), 250 ng of cDNA was used for each qRT-PCR reaction containing HOT FIREPol EvaGreen qPCR Supermix (Solis Biotec). qRT-PCR was performed using the CFX384 Touch Real-Time PCR Detection System (BioRad) with the following settings: initial denaturation (95°C for 12 min) followed by 38 cycles of denaturation, annealing and extension (95°C for 15 s, 60°C for 20 s and 72°C for 20 s, respectively). Target genes were normalized to the average of house-keeping genes *Rn18s* and *Gapdh*, and changes in gene expression were determined using the $\Delta\Delta C_t$ method. For sequences of primers used, see [Table S1](#).

Gapdh F: ACAGCCGCATCTTCTTGTGCAGTG.
Gapdh R: GGCCTTGACTGTGCCGTTGAATTT.

Measurement of mtDNA copy number

Cells were seeded in 60 mm Petri dish at a density 0.5×10^5 cells per dish, one day prior to DNA extraction. Genomic DNA was extracted from cells using the Wizard Genomic DNA Purification Kit following the manufacturer's protocol. The purity and concentration of the DNA was assessed by NanoDrop instrument (Thermo Fisher Scientific). To detect the expression of both nuclear and mitochondrial DNA, 100 ng of genomic DNA was utilized for each qPCR reaction, which included HOT FIREPol EvaGreen qPCR Supermix (Solis Biodyne). The measurement was conducted using the CFX96 Touch Real-Time PCR Detection System (BioRad) with the following parameters: initial denaturation (95°C for 12 min) followed by 38 cycles of denaturation, annealing and extension (95°C for 15 s, 60°C for 20 s and 72°C for 20 s, respectively). The expression level of mtDNA was subsequently normalized to the level of nuclear DNA using the $\Delta\Delta C_t$ method. For detection of mitochondrial DNA, mMito1 primers and for detection of nDNA m18SRNA primers were used, see [Table S1](#).

Quantification of mtDNA nucleoids

Cells were seeded onto microscopy coverslips (Paul Marienfeld) and cultured under standard conditions for a minimum of 24 h, followed by 15 min fixation with 4% PFA, washing with PBS, permeabilization 15 min with 0.1M glycine, 0.05% Triton X-100, 0.05% Tween 20 in PBS. Subsequently, cells were washed 3x with PBS, blocked for 30 min with BSA and labeled with anti-Tom20 (Santa Cruz Biotechnology) and anti-DNA antibody (Sigma-Aldrich) followed by 5 × 5 min washing with 0.05% Saponin in PBS, labeling with corresponding secondary antibodies (Abberior) and washing with 3 × 5 min with 0.05% Saponin in PBS. After washing with H₂O, samples were mounted in Vectashield (Vector Laboratories) and imaged on Nikon CSU-W1 confocal microscope. The amount of mtDNA was quantified in FIJI¹⁰¹ as a number of mtDNA nucleoids normalized to the mitochondrial (Tom20-positive) area.

In vivo experiments

Various mouse strains were grafted subcutaneously with B16, B16 Miro1^{KO}, B16 ρ^0 , B16 ρ^0 Miro1^{KO}, B16 ρ^0 GFP cells, or cells derived from B16 ρ^0 tumors (D10, D15 and D20) at 10^6 cells per 100 μ L of PBS. Tumor volume was measured using calipers. For fluorescent cytometry analysis and microscopy, tumors were harvested on different days post-tumor cell injection (day- D5, D10, D15, and D20) and processed for single-cell populations (fluorescent cytometry) or subjected to various microscopy techniques as described below.

To detect double-positive cells by fluorescent cytometry, tumor plaques from B16 ρ^0 GFP cells were dissected, cut into small pieces, and minced using 70 μ m cell strainer. The cellular suspension was washed with cold PBS, centrifuged at 300g/5 min, and resuspended in FACS buffer (PBS +2% FBS). Hoechst 33258 (10 μ g/mL) was used to assess cell viability. Fluorescent cytometry detection of double-stained population of GFP⁺/mKate2⁺ was performed using BD Fortessa with detection of GFP/PE positivity. The FACS setting and gating strategy were established using controls with no fluorescence, GFP-only or mKate2-only fluorescence samples. Microscopy detection was managed according to the methods described below.

The offspring generation of crossbreeding between the Rhot1 Rosa-CreERT2 mouse and a reporter transgenic mouse expressing dTomato/EGFP fluorescence was either induced or uninduced with tamoxifen as described in Animal models. Mice were then grafted s.c. with B16 melanoma cells at 10^6 to Ctrl and Miro1^{KO} mice and tumor samples were collected after 14 days. Tumors were fixed in 2% PFA O/N, soaked with 30% sucrose (Serva) solution, snap-frozen in OCT (VWR) and stored at -80°C . Cryosections (5–10 mm thick) were cut using a cryomicrotome (Leica) and mounted in Mowiol (Sigma-Aldrich) with Hoechst 33342 (Sigma-Aldrich). Samples were imaged by confocal microscopy (Leica TCS SP8 WLL SMD-FLIM) and images analyzed by FIJI.

Imaging of tumor sections and analysis of mitochondrial transfer

For the purpose of microscopic detection, whole resected tumors were fixed in 2% PFA for 12–24 h, soaked with 30% sucrose (Serva) solution, snap-frozen in OCT (VWR) and stored at -80°C . Cryosections (5–10 mm thick) were cut using a cryomicrotome (Leica) and mounted in Mowiol (Sigma-Aldrich) with Hoechst 33342 (Sigma-Aldrich).

Samples were imaged on a Nikon Eclipse Ti2 microscope (Nikon). From each section three to five fields of view (FOV, size 133.12 × 133.12 μ m with z-spacing 0.3 μ m) containing both GFP and mKate2 signals were imaged and processed in FIJI.

Isolation of mitochondria

Mitochondria were isolated from both cells and mouse organs. For the isolation of mitochondria from cells was used STE buffer (250 mM sucrose, 1 mM EDTA, 10 mM Tris pH 7.6). Cells were at first collected to ice-cold PBS and centrifuged 500 rcf/5 min/ 4°C . The cell pellet was homogenized with Balch-style homogenizer (Isobiotec) and mitochondria isolated by stepwise rounds of centrifugation (800 rcf then 3000 rcf 10 min each at 4°C) with final centrifugation at 10,000 rcf/15 min/ 4°C . The mitochondrial pellet was resuspended in STE buffer and concentration estimated using BCA assay (Thermo Fisher Scientific). For isolation of mitochondria from mouse liver from C57BL/6 mice tissue homogenization buffer (20 mM HEPES-KOH pH 7.4, 220 mM Manitol, 70 mM Sucrose, 1mM EDTA) was used. Extracted tissues were washed with 1x PBS on ice. A slice of tissue was cut into small pieces and incubated in homogenization buffer on ice for 15 min. Tissue slices were manually disrupted using a Dounce tissue grinder and pestle

(Kimble). The resulting homogenate was processed by Balch-style homogenizer and sample prepared as described above. The mitochondrial pellet was washed 3x with STE buffer, re-suspended in the same, and protein concentration was determined by the BCA assay (Thermo Fisher). Mitochondria were kept on ice and used within 4h in microscopy experiments. The final concentration of mitochondria used in experiments was 50 $\mu\text{g}/\text{mL}$ for all experiments involving landing rate quantification in TIRF microscopy (see below).

TUNEL assay

Tumors were collected at the endpoint of tumor volume measurement (14 days for B16 and 30 days for B16 ρ^0 cells). Whole resected tumors were fixed in 4% formaldehyde, soaked with 30% sucrose (Serva) solution, snap-frozen in OCT compound (VWR) and stored at -80°C . Four-micron cryosections were cut on a cryomicrotome (Leica). TUNEL assays were performed according to the manufacturer's instruction by *In Situ* Cell Death Detection Kit (Roche). All sections were mounted in Mowiol (Sigma-Aldrich) with Hoechst 33342 (5 $\mu\text{g}/\text{mL}$) (Sigma). The fraction of apoptotic cells was quantified in FIJI as the number of TUNEL (fluorescein) positive nuclei divided by the total number of nuclei (Hoechst).

Analysis of mitochondrial positioning using CYTOO chips

For analysis of mitochondrial positioning, we used Y-shaped micropatterned culture coverslips (CYTOO SA). One million harvested cells were incubated with 100 nM MitoTracker Deep Red (Thermo Fisher Scientific) for 30 min in the dark, washed twice with PBS and diluted to the concentration of 1.5×10^4 cells/mL. In total, 6×10^4 cells per chip were seeded on the CYTOO chip and cultured for 3–4 h to spread into Y patterns. Cells were washed three times with PBS, fixed for 15 min with 2% formaldehyde at 37°C , permeabilized using 0.1% Triton X-100, 0.05% Tween 20 and 0.1M glycine in PBS for 5 min, then washed two times with PBS and labeled 30–60 min with 165nM Alexa Fluor 488 conjugated Phalloidin (Thermo Fisher Scientific). Labeled cells were washed two times with PBS, once with distilled water, air dried and mounted in Mowiol (Sigma-Aldrich) with Hoechst 33342 (5 $\mu\text{g}/\text{mL}$) (Sigma-Aldrich).

Cells in patterns were imaged on the Nikon Eclipse Ti2 microscope (Nikon) and fluorescence was excited with 405, 488 and 640 nm lasers. For each cell, the z stack was adjusted to capture the whole cell with a z-step size of 0.3 μm .

The distribution of mitochondria within cells was quantified in FIJI by the Sholl-based analysis approach as described previously.³⁸ Briefly, for each cell, the maximum intensity projection (MIP) image was created, and the mitochondria were segmented based on the MitoTracker signal. The cumulative area occupied by mitochondria was quantified in subsequent one micrometer wide shells radiating from the nuclei border toward the cell periphery. Distance (the shell) in which 95% of the mitochondrial area is localized (Mitochondria⁹⁵ value) was extracted for each cell. MIP of individual cells or average intensity projection of MIP of analyzed cells were visualized by FIJI.

Analysis of mitochondrial network dynamics

Cells were seeded into a 35 mm glass bottom Petri dish (Cellvis) and cultured under standard conditions for a minimum of 24 h. In all but mito::mKate2 cells the mitochondria were labeled with 100 nM MitoTracker Deep Red (Thermo Fisher Scientific) for 30 min in the dark and washed with PBS. The mitochondria were imaged under a standard culture condition on a Nikon Eclipse Ti2 microscope (Nikon). The movement of mitochondria was captured in 60 subsequent time points with 1 s (for cancer cells) or 5 s (for MSCs) intervals. The dynamic of a mitochondrial network was quantified as a fraction of mitochondria which changed their position within two subsequent time points.³⁸ Median values from all time points were calculated for each cell.

Quantification of mitochondrial movement in cell-free reconstituted system

Motor protein kinesin KIF5B was prepared as described previously.^{62,63} Briefly, the cDNA was PCR amplified using primers containing *Ascl*- and *NotI*-digestion sites flagging given KIF5B-encoding nucleotide sequences (forward primer AAT AAT AAC ATG CGG CCG CAA TGG CGG ACC TGG CCG AGT G, reverse primer AAT AAT AAC ATG GCG CGC CTG CTT CCT TTA TGC GAT CTA CTT CTT GC). After *Ascl*- *NotI*-digestion of inserts and FlexiBAC expression vector,¹⁰² containing C-terminal GFP tag followed by a 3C PreScission protease cleavage site and a 6xHis-tag, ligation reaction followed. Construct was expressed in SF9 insect cells (Expression systems). The insect cells were harvested (300 rcf for 10 min at 4°C) and stored resuspended in PBS at -80°C for further use. Insect cells were lysed by homogenization in 30 mL ice-cold His-Trap buffer (50 mM Na-phosphate buffer, pH 7.5, 5% glycerol, 300 mM KCl, 1 mM MgCl_2 , 0.1% tween 20, 10 mM BME, 0.1 mM ATP) with 30mM imidazole, protease inhibitor cocktail (Roche) and benzonase (25 U/mL), and centrifuged at 45 000 rcf for 60 min at 4°C . Cell lysate was loaded on Ni-NTA column (Thermo Fisher Scientific, 2 h at 4°C), washed with wash buffer (His-Trap buffer supplemented with 60 mM imidazole) and the protein was eluted with elution buffer (His-Trap buffer supplemented with 300 mM imidazole). The purification tag was cleaved overnight by 3C PreScission protease. The solution was reloaded onto a Ni-NTA column to further separate the cleaved protein from the 6xHis-tag. The protein was concentrated using an Amicon ultracentrifuge filter and flash frozen in liquid nitrogen.

Adaptor protein mCherry-TRAK1 was prepared as described previously.⁶² Briefly, desired sequences of mCherry-TRAK1 cDNA were PCR amplified using specifically designed primer pairs (step 1 forward primer: TCG GAG AAC CTG TAC TTC CAG TCT ACC ATG GTG AGC AAG GGC GAG GAG GAT AAC ATG, step 1 reverse primer: GGG GAC CAC TTT GTA CAA GAA AGC TGG GTT ATT ACC GTA AGC TAG TTT GTT TGG AGA G, step 2 forward primer: GGG GAC AAG TTT GTA CAA AAA AGC AGG CTC GGA GAA CCT GTA CTT CCA G, step 2 reverse primer: GGG GAC CAC TTT GTA CAA GAA AGC TGG GTT ATT ACC GTA AGC TAG TTT GTT TGG AGA G). Gateway entry clone was generated by insertion of nucleotide sequence by means of a BP recombinant

reaction according to the manufacturer's protocol into a pDONR221 donor vector and verified by Sanger sequencing. Expression plasmid was generated by an LR recombinant reaction resulting in a destination vector containing a TEV-cleavage site and a TwinStrep-FLAG-Halo-tag at the N terminus of TRAK1. Construct was expressed in HEK293T cells (a kind gift from Radu A. Aricescu, University of Oxford, England),¹⁰³ grown in Free Style F17 medium (Gibco) with 0.1% Pluronic F-68 and 2mM L-glutamine at 110 rpm under a humidified 5% CO₂ atmosphere at 37°C. In all, 1 mg/mL linear polyethylene imine (Polysciences) and 0.7 mg of the expression plasmid were incubated in PBS for 10 min prior to the addition to 350 mL cells at the concentration of 4×10^6 cell/mL. 4 h post-transfection, the cells were diluted 2-fold in ExCell serum-free medium. Four days post-transfection, the cells were harvested by centrifugation at 4°C for 10 min at 500 rcf. The cell pellet was resuspended in ice-cold lysis buffer (100 mM Tris-HCl, 10 mM NaCl, 5 mM KCl, 2 mM MgCl₂, 10% glycerol, pH 8.0) with benzonase (1 U/mL; Merck) and Complete protease inhibitor cocktail (Roche) and lysed by pulsed sonication for 5 min (20 s pulses with 24W/min) assisted by the addition of Igepal-630 to the final concentration of 0.2% (v/v) during 20 min incubation on ice with occasional mixing. After addition of NaCl (final conc. 150mM) mixture was incubated 20 min on ice and centrifuged (9000 g, 15 min, 4°C) to remove insoluble material followed by a second centrifugation step (30 000 g, 30 min, 4°C). The supernatant was loaded onto a StrepTactin XT column (IBA) equilibrated in lysis buffer with 150mM NaCl for affinity chromatography, followed by column washing with wash buffer (100mM Tris-HCl, 150mM NaCl, 1mM EDTA, pH 8), the protein was eluted by cleaving off the N-terminal tag with 1:20 (w/w) TEV protease in the wash buffer O/N at 4°C. Eluted protein was collected and concentrated using an Amicon ultracentrifuge filter (cutoff of 100 kDa, Merck), loaded onto a Superose 6 10/300 GL column (Merck) and separated by size exclusion chromatography with 100mM Tris-HCl pH 8.0, 150mM NaCl, 2mM MgCl₂, 1mM EDTA, 0.1% tween, 10% glycerol, 1mM DTT, 0.1mM ATP as a mobile phase. The purified protein was concentrated using an Amicon ultracentrifuge filter and flash frozen in liquid nitrogen.

Microtubules were prepared by polymerization of 4 mg/mL porcine tubulin in BRB80 (80 mM PIPES, 1 mM EGTA, 1 mM MgCl₂, pH 6.9) buffer supplemented with 1 mM GMPCPP and 1 mM MgCl₂ in 37°C for 2 h after 5 min depolymerization on ice. Polymerized microtubules were centrifuged for 30 min at 18 000 rcf and carefully resuspended in 100–200 μ L BRB80 supplemented with 10 μ M taxol (BRB80T). Mitochondria were isolated as described.

Chambers for IRM/TIRF imaging of reconstituted system were assembled from cleaned (H₂O₂/H₂SO₄) and silanized (0.05% dichlorodimethylsilane) 18 x 18 and 22 x 22 mm coverslips separated with four parallel stripes of parafilm in between and sealed on a heating plate (60°C) creating four separated channels for imaging. Each channel is flushed with 40 μ L of PBS, incubated with 20 μ L of anti- β -tubulin antibody (Sigma) for 10 min and with 40 μ L of Pluronic F-127 for at least 1 h. Just before imaging, the channel was flushed with 40 μ L of BRB80T, followed by 8 μ L of microtubule solution. After 30 s the unbound microtubules are washed away by flushing channel with 20 μ L of BRB80T and 20 μ L of motility buffer (BRB80 with 10 μ M taxol, 10 mM dithiothreitol, 20 mM D-glucose, 0.1% Tween 20, 0.5 mg/mL casein and 1 mM ATP) with freshly added glucose oxidase (0.22 mg/mL) and catalase (0.02 mg/mL). Lastly, the isolated mitochondria (50 μ g/mL), kinesin (20 nM) and TRAK (20 nM) were diluted in 20 μ L of motility buffer with glucose oxidase and catalase, incubated on ice for 10 min and flushed into the channel for imaging of mitochondria movement.

Interference reflection microscopy (IRM) imaging was done on an inverted widefield Nikon Eclipse Ti-E microscope equipped with an H-TIRF module. All samples were imaged in IRM mode for 120 s in one or a half second intervals. Both the microtubules and mitochondria were identified based on contrast on IRM data. Only the microtubules stably attached for the whole duration of the acquisition were considered. Single mitochondria were identified based on their appearance as bright spots on black background, size around one micrometer, round shape, and presence on more than two consecutive images. The parameters of movement (distance traveled, velocity and interaction time) were calculated in Excel (Microsoft) based on coordinates of kymographs created in FIJI software. The landing rate (number of mitochondria interacting with microtubules) was calculated as the total number of mitochondria (either all or just processive ones) associated with microtubules normalized to time and microtubule length.

Correlative light and electron microscopy

MSCs with mKate2 tagged mitochondria were seeded (10^5 cells/well) in a 35mm dish with a gridded coverslip (Mattek). Cells were cultured for 48 h and subsequently imaged under standard culture conditions on a Nikon Eclipse Ti2 microscope (Nikon) for localization of TNTs containing mitochondria. After imaging, the samples were postfixed with 2.5% glutaraldehyde (GA) and 1% formaldehyde (FA) in 0.1M sodium cacodylate buffer (CDS) for 1 h on ice. Cells were then washed with the same buffer (3x, 5 min), post-fixed in reduced 1% OsO₄ with 1.5% K₃(FeCN)₆, then in 1% OsO₄ (both in 0.1M CDS, 30 min, on ice), washed with the fixation buffer, distilled H₂O, and contrasted with 1% uranyl acetate in H₂O (30 min, no light, room temperature). After H₂O wash samples were dehydrated with ethanol (30%, 50%, 80%, 95%, 100%, 2 min each, except 5 min in 100%) and embedded in Embed812. Samples were mounted on regular SEM stubs using conductive carbon and coated with 25 nm of platinum (using High Vacuum Coater, Leica ACE600).

Electron tomograms were captured using focus ion beam scanning electron microscopy (FIB-SEM) FEI Helios NanoLab 660 G3 UC. The target cells were localized based on grid coordinates. On top of localized TNTs connected to target cells, a protective layer of platinum (1000 nm) was deposited. A large trench around the protected region was milled. SEM images were acquired at 2 kV, 0.2 nA, using the Elstar in-lens BSE detector (TLD-BSE) and in-column backscattered electron detector (ICD) with pixel size 3 nm and a pixel dwell time 35–50 μ s.

The stacks of images were aligned and denoised with median filter in Amira software. The surface of TNTs and mitochondria were automatically segmented with pretrained neural network in NIS Elements software. Tubulin fibers were segmented using a manual tracking in Amira software (better visibility in YZ axis). For the final visualization of the 3D model the Imaris software was used.

Transmission electron microscopy

Cells were seeded on microscopy coverslips and processed as monolayers, or in culture plates and processed as a 2% low melting agarose embedded suspension. Cells were fixed with the mixture of 2% formaldehyde and 2.5% glutaraldehyde in 0.1M PHEM buffer, postfixed and contrasted for 1 h with 1% osmium tetroxide and 1.5% potassium hexacyanoferrate(III) and for 30 min with 1% uranyl acetate, dehydrated by series of diluted ethanol (30%, 50%, 70%, 80%, 90% and 100% solutions) followed by acetone incubation, and embedded in Epon epoxy resin for sectioning. 70 nm sections were cut on Ultramicrotome Leica EM UC7 and imaged on transmission electron microscope JEOL JEM 2100-Plus 200kV. For each sample, at least ten different fields of view from different cells were captured and analyzed. Mitochondria and cristae area were measured manually in FIJI.

Microfluidic co-cultures of cells

To spatially separate two populations of co-cultured cells, we used a custom-made microfluidic device with two separated channels (see Figure S4A). The device was manufactured by casting the SYLGARD 184 Silicone Elastomer Kit (Dow) on a reusable master mold. The master mold was prepared by spin-coating SU-8 2075 photoresist (MicroChem) on a 3-inch silicon wafer (Microchemicals). After soft-baking at 95°C, the photoresist was exposed using mercury lamp and custom-shaped photolithographic mask (Compugraphics). The negative mold pattern was then developed by sonication in PGMEA (Sigma-Aldrich). Cleaned and sterilized devices were placed in glass bottom Petri dishes, and both channels were first filled with FBS for 30 min, followed by flushing with cell suspensions (2.5×10^4 cells/ μ l). To enhance cell attachment, the dishes were centrifuged at 200 rcf for 3 min and incubated for 45 min under standard culture conditions. After removal of the device, unattached cells were carefully washed with PBS and co-cultures incubated for the desired time. As necessary, MSCs were labeled 24 h before use with MitoTracker Deep Red (Thermo Fisher Scientific) according to manufacturers' instructions. Cocultures were imaged with Leica DMI8 widefield microscope equipped with HC PL APO 63x objective.

Analysis of mitochondrial presence in TNTs of MSCs

MSCs isolated from mito:mKate2 mice were seeded in a glass bottom microscopy Petri dish (10^5 per well), cultured for 48 h, and subsequently imaged under standard culture conditions on a Nikon Eclipse Ti2 microscope (Nikon). Regions of interest (ROIs) containing TNTs were selected based on bright field imaging (blind to mitochondrial signal). Selected ROIs were subsequently imaged in brightfield (for further identification of TNTs) and in fluorescence (for quantification of the mitochondrial mKate2 signal). The fraction of TNTs occupied by mitochondria was calculated as length of part of TNT positive for mitochondrial fluorescence divided by total length of the TNT.

Scheme design

The schemes in Figures 1A, 2A, and 4A were created utilizing elements from Servier Medical Art (Creative Common Attribution 3.0 Generic License, www.smart.servier.com).

QUANTIFICATION AND STATISTICAL ANALYSIS

Graphs and statistics were performed using GraphPad Prism 8 software. Data were analyzed as following, for comparison of more groups one-way ANOVA (Dunnett's or Tukey multiple comparison tests) or two-way ANOVA (Sidak test) were used. When comparing 2 groups, paired or unpaired t test was used. Data are presented as mean values \pm SEM. The difference was considered statistically significant on level of $p < 0.05$ with p values indicated in graphs as follows * $p < 0.05$, ** $p < 0.01$, *** $p < 0.001$, **** $p < 0.0001$.